Journal of Structural Biology 215 (2023) 107993

Contents lists available at ScienceDirect

Journal of Structural Biology

journal homepage: www.elsevier.com/locate/yjsbi

Advances in computational approaches to structure determination of alphaviruses and flaviviruses using cryo-electron microscopy

Kiran Lata [a], Sylvia Charles [a], Vidya Mangala Prasad [a,b,*]

[a] Molecular Biophysics Unit, Indian Institute of Science, Bengaluru, Karnataka 560012, India
[b] Center for Infectious Disease Research, Indian Institute of Science, Bengaluru, Karnataka 560012, India

ARTICLE INFO

Edited by 'Bauke W. Dijkstra'

Keywords:
Cryo-electron microscopy
Icosahedral Envelope virus structure
3D image reconstructions
Near-atomic resolution
Alphaviruses
Flaviviruses

ABSTRACT

Advancements in the field of cryo-electron microscopy (cryo-EM) have greatly contributed to our current understanding of virus structures and life cycles. In this review, we discuss the application of single particle cryo-electron microscopy (EM) for the structure elucidation of small enveloped icosahedral viruses, namely, alpha- and flaviviruses. We focus on technical advances in cryo-EM data collection, image processing, three-dimensional reconstruction, and refinement strategies for obtaining high-resolution structures of these viruses. Each of these developments enabled new insights into the alpha- and flavivirus architecture, leading to a better understanding of their biology, pathogenesis, immune response, immunogen design, and therapeutic development.

1. Introduction

Viruses are infectious particles that parasitize almost every living system: prokaryotes and eukaryotes. They cause enormous health burdens to humans, plants, and animals, notwithstanding economic burdens to nations worldwide. A virus particle simply comprises a genome, either single- or double-stranded RNA or DNA molecule(s) protected by a protein capsid. The capsid shell can be a single layer, as in the case of rhinoviruses (Rossmann et al., 1985) and enteroviruses (Plevka et al., 2012), or multiple capsid shells, such as paramecium bursaria chlorella virus (PBCV) (Fang et al., 2019) and faustovirus (Klose et al., 2016). In addition, virus particles can be with or without a membrane bilayer enclosing the viral genome. Viruses with a lipid envelope surrounding the capsid and viral genome are called enveloped viruses, including viruses such as alphaviruses (Jose et al., 2009), flaviviruses (Kuhn et al., 2002), coronaviruses (Yao et al., 2020), and filoviruses (Bharat et al., 2012). Viruses that lack a lipid envelope have either a helical or spherical (icosahedral symmetry) structure, but having a lipid envelope allows viruses to deviate from strict symmetrical architectures and accommodate variable shapes, such as with rubella virus (Battisti et al., 2012; Mangala Prasad et al., 2017), influenza virus (Noda, 2011), ebola virus (Bharat et al., 2012) and hepatitis B virus (Crowther et al., 1994). Every virus also has a virus attachment factor entrenched in its outermost layer (capsid layer in non-enveloped viruses and lipid bilayer in enveloped viruses) that facilitates the attachment of the virus to its host cell (Louten, 2016).

The three-dimensional (3D) structure of viruses can provide mechanistic insights into the viral life cycle, which can provide a roadmap to design effective vaccines and antivirals (Chiu and Schmid, 1997). Different methods have been used to determine viral structures depending on virus morphology. Major techniques have been x-ray crystallography, x-ray fiber diffraction, cryo-electron microscopy (cryo-EM), and cryo-electron tomography (cryo-ET). X-ray crystallography has successfully been used to determine the structures of icosahedral viruses since the 1970s. The earliest virus structures solved using x-ray crystallography were of icosahedral plant viruses (Abad-Zapatero et al., 1980; Harrison et al., 1978; Liljas et al., 1982) followed by structures of animal viruses such as human rhinovirus (Rossmann et al., 1985), and poliovirus (Hogle et al., 1985). Similarly, viruses with helical symmetry such as tobacco mosaic virus have been studied using X-ray fiber diffraction (Namba and Stubbs, 1986). X-ray methods work well for viruses that can form a crystalline lattice or fibers. However, due to the inherent flexibility of membrane bilayers, these methods give limited results for the structure determination of enveloped viruses as these viruses rarely yield long-range, ordered lattices. With the development and application of transmission electron microscopy (TEM) methods to biological samples, low-resolution structures of icosahedral viruses could be determined from two-dimensional projection images. As TEM does not require ordered stacking of virus particles, it became an attractive tool to study enveloped viruses (Crowther et al., 1970b).

* Corresponding author.

https://doi.org/10.1016/j.jsb.2023.107993
Received 16 March 2023; Received in revised form 15 May 2023; Accepted 3 July 2023
Available online 4 July 2023

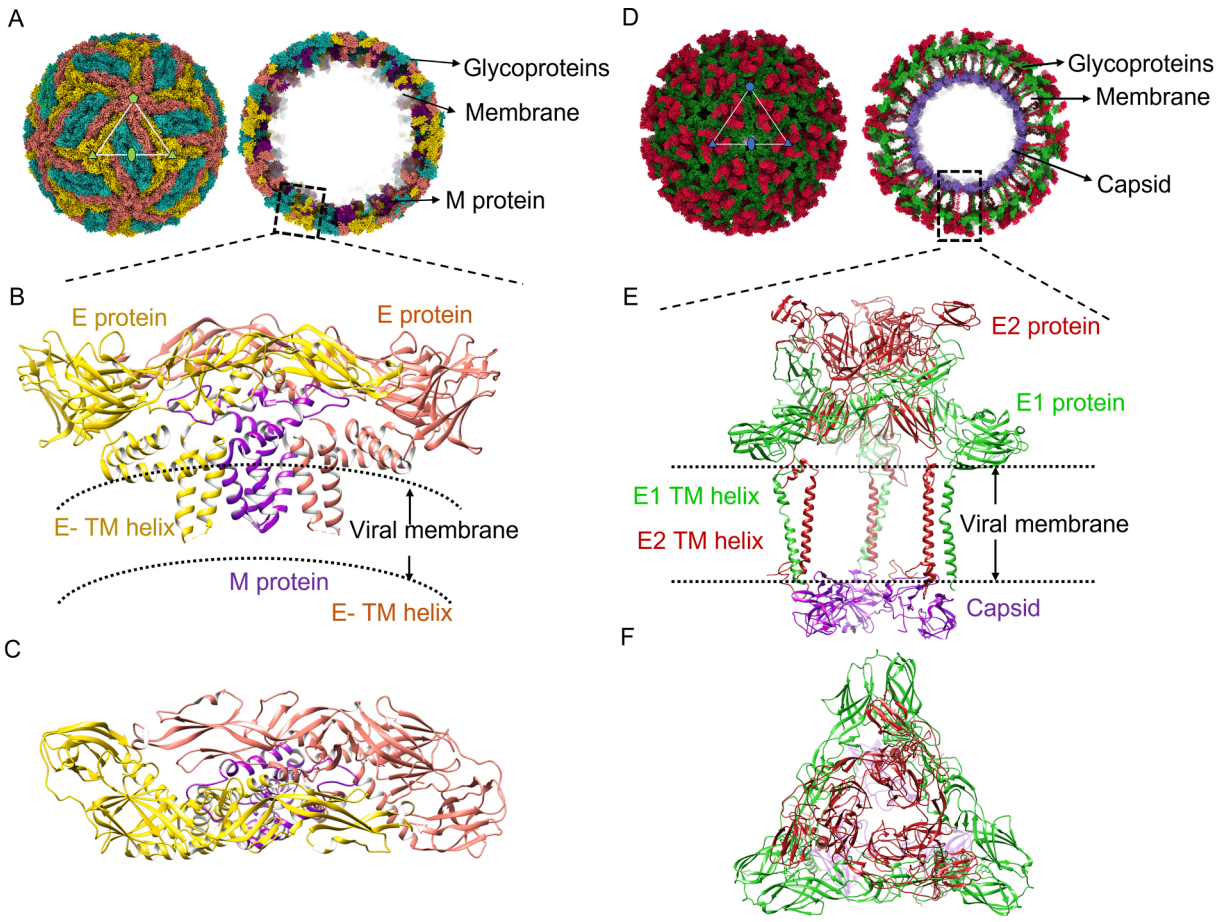

Fig. 1. (A) General architecture of flavivirus, Surface view (Left) and central slab view of flavivirus (Right); (B) Organization of E (Yellow and coral) and M (purple) protein dimers as present on flavivirion surface (lateral view); (C) Top view of antiparallel E protein dimer. (D) General architecture of alphavirus, Surface view and central slab view of alphavirus (Right); (E) Organization of E1 (green), E2 (red), Capsid (purple) proteins across the lipid bilayer of an alphavirus (lateral view); (F) Top view of a trimeric glycoprotein spike as present on alphavirions. PDB ID 7KV8 and 6NK7 were used for making figures for flavivirus and alphavirus structures respectively. Five-fold, three-fold, and two-fold icosahedral symmetry axes on the virus structure are represented by pentagon, triangle and oval in panels A and D. Figures were generated using UCSF Chimera (Pettersen et al., 2004) and UCSF ChimeraX (Goddard et al., 2018). (For interpretation of the references to colour in this figure legend, the reader is referred to the web version of this article.)

Development of TEM sample vitrification (Adrian et al., 1984; Chiu et al., 1986; Dubochet et al., 1982a) avoided artifacts, such as dehydration, induced due to heavy metal staining of biological samples leading to the use of cryogenic transmission electron microscopy (cryo-TEM or more commonly referred to as cryo-EM) to determine enveloped virus structures. However, it was still imperative that the virion particles were symmetrical and identical in shape and size. Thus, initial structures of enveloped viruses that were determined were of symmetrical alphaviruses, Semliki Forest virus (SFV; 35 Å) (Vogel et al., 1986), Sindbis virus (SINV; 35 Å) (Fuller, 1987; Paredes et al., 1993), followed by herpes simplex virus 1 nucleocapsid structure (HSV1; 40 Å) (Schrag et al., 1989).

Though low resolution cryo-EM structures of symmetrical, enveloped viruses could be determined, elucidation of protein arrangement in the structures was possible only by fitting crystal structures of respective viral proteins in the cryo-EM density maps. Availability of crystal structures for the surface glycoproteins of alphaviruses (Lescar et al., 2001) and flaviviruses (Rey et al., 1995) as well as capsid protein of alphaviruses (Choi et al., 1991; Lee et al., 1996) enabled interpretation of low-resolution cryo-EM structures of both alphaviruses (Mukhopadhyay et al., 2006; Zhang et al., 2002) and flaviviruses (Kuhn et al., 2002). Using crystal structures to interpret cryo-EM map density became the established way of elucidating cryo-EM structures of viruses as it is not possible to trace protein chains in density maps >5 Å (Baker et al., 2007). Subsequent technological advancements in biological cryo-EM methods through the last four decades have now made it possible to determine enveloped virus structure determination to near-atomic resolutions (Hardy et al., 2021; Khare et al., 2021; Newton et al., 2021; Renner et al., 2021a; Wang et al., 2022b; Wang et al., 2022c). The present review focuses on computational cryo-EM structure determination of small, enveloped, spherical viruses with icosahedral symmetry, namely, flaviviruses and alphaviruses, which have been studied extensively due to their enormous global health burdens and symmetrical structure properties.

Flavi- and alphaviruses are arthropod-borne viruses causing severe diseases in humans and other animals with a wide geographical span. Flaviviruses such as dengue virus (DENV) cause more than 100 million infections yearly characterized by fever, vomiting, and joint and muscle pain. In severe cases, dengue infections can also lead to life-threatening conditions known as dengue hemorrhagic fever or dengue shock syndrome (Carod-Artal et al., 2013; Halstead, 2007). Other flaviviruses such as Japanese encephalitis virus (JEV) (Griffiths et al., 2014; Rosen, 1986), and West Nile virus (WNV) (Petersen et al., 2013; Suthar et al., 2013) cause encephalitis in humans. Zika virus (ZIKV) causes congenital microcephaly (Brasil et al., 2016; Honein et al., 2017; Plourde and Bloch, 2016) and Guillain-Barre' syndrome in adults (Cao-Lormeau et al., 2016; Passi et al., 2017). Tick-borne encephalitis virus (TBEV causes 13,000 cases of human meningitis and encephalitis annually

(Bogovic and Strle, 2015). Alphaviruses such as chikungunya (CHIKV) (Silva and Dermody, 2017), Ross River virus (RRV) (Farmer and Suhrbier, 2019), Mayaro virus (MAYV) (Taylor et al., 2005), getah virus (GETV) (Liu et al., 2019), O'nyong nyong virus (ONNV) (Rezza et al., 2017), and SINV (Adouchief et al., 2016) induce myalgia and fever-rash-arthralgia conditions (Suhrbier et al., 2012). Furthermore, eastern equine encephalitis virus (EEEV) (Deresiewicz et al., 1997), western equine encephalitis virus (WEEV) (Centers for Disease Control and Prevention CDC, 1995), and Venezuelan equine encephalitis virus (VEEV) (Weaver et al., 2004) cause encephalitis and severe neurological diseases in humans and some animals (Aréchiga-Ceballos and Aguilar-Setién, 2015).

Both flaviviruses and alphaviruses are icosahedral membrane-enveloped viruses with similarly sized positive-sense single-stranded RNA genomes. Their positive sense RNA genomes are in complex with the viral capsid protein and surrounded by a lipid bilayer decorated with heterodimers of their respective glycoproteins (Fig. 1**A and 1D)** (Kuhn et al., 2002; Von Bonsdorff and Harrison, 1975). The fusion glycoprotein of flaviviruses (E) (Rey et al., 1995), and alphaviruses (E1) (Lescar et al., 2001) share a similar overall fold and are both triggered for membrane fusion by low pH conditions (Allison et al., 1995; Wahlberg and Garoff, 1992), but their arrangement on virion surface is significantly different (Pulkkinen et al., 2022; Wang et al., 2022b). Detailed reviews on alpha- and flavivirus biology, structure, proteins, and life cycle have been previously published (Button et al., 2020; Hasan et al., 2018a; Hernandez et al., 2014; Jose et al., 2009; Kuhn, 2013; Mukhopadhyay et al., 2005; Griffin, 2013; Sirohi and Kuhn, 2017). Thus, in this review, only a general overview is provided on these aspects.

Mature flavivirus structures contain 180 copies each of its envelope glycoprotein (E) and membrane protein (M) forming heterodimers. These are arranged as 90 dimers that lie laterally on the mature virion surface in an icosahedral fashion following T = 3 quasi-symmetry with each asymmetric unit consisting of 3 heterodimers of E and M (Kuhn et al., 2002) (Fig. 1A, 1B & 1C). The inner capsid shell that encloses the genome does not align with the surface glycoproteins symmetry and likely forms an asymmetric nucleocapsid core (Kuhn et al., 2002; Prasad et al., 2017; Therkelsen et al., 2018). Flaviviruses enter cells through receptor-mediated endocytosis and deliver their genomic material into the cytoplasm through virus membrane fusion with endosomal membranes at low pH. Once released in the cytosol, the RNA genome is translated into a single polyprotein by the host translation machinery. The polyprotein is further processed into functional proteins by either viral or host-encoded proteases in the endoplasmic reticulum (ER). Assembly of flavivirus occurs on the ER membrane where the capsid proteins in association with newly replicated viral genome on the cytoplasmic side buds into the ER lumen along with the membrane-anchored E and precursor membrane (prM) glycoproteins forming the virion surface (Byk and Gamarnik, 2016). The newly assembled, immature virions have 60 trimeric spikes of prM-E heterodimer arranged on their surface in an icosahedral pattern (Kostyuchenko et al., 2013; Prasad et al., 2017; Zhang et al., 2003b) giving it the spiky appearance typical of immature flavivirions. Glycosylation of prM and E proteins occurs in the *trans*-Golgi network (TGN) along with proteolytic cleavage of prM to pr and M proteins. In the TGN, immature flavivirions undergo major conformational changes to form mature flavivirions with a smooth surface appearance (Fig. 1**A, 1B & 1C),** which are subsequently released out of the cell by exocytosis (Hasan et al., 2018a; Kuhn et al., 2002). The pr peptide dissociates from the virion surface after exocytosis, leaving only E and M proteins on mature virion surface (Yu et al., 2008).

In contrast, alphaviruses contain an outer glycoprotein layer with 240 copies each of its surface glycoproteins, E1 and E2. Heterodimers of E1 and E2 are arranged as 80 trimeric spikes in an icosahedral, T = 4 pattern with each asymmetric unit comprising 4 E1-E2 heterodimers (Hasan et al., 2018b; Kuhn, 2007; Sun et al., 2013; Tellinghuisen et al., 2001). The inner capsid shell in the virion also forms an icosahedron with T = 4 arrangement similar to the outer glycoprotein surface (Fig. 1D, 1E & 1F). Alphaviruses, like flaviviruses, enter host cells via receptor-mediated endocytosis and release their nucleocapsid into the cytosol by membrane fusion in acidic endosomal compartments. Upon genome release, a 26S subgenomic mRNA is translated into a polyprotein containing its structural proteins (Kuhn, 2013; Strauss et al., 1984; Griffin, 2013; Strauss and Strauss, 1994). The translated glycoproteins are assembled in the ER and are cleaved by virus or host encoded-proteases. The capsid protein is autocatalytically cleaved and encapsulates newly replicated RNA genomes forming nucleocapsid cores in the cytoplasm. The translated glycoproteins are transported to the plasma membrane via ER and TGN, during which the glycoproteins are glycosylated and the precursor form of E2 glycoprotein (pE2) is proteolytically cleaved into E2 and E3 (Holmes et al., 2020; Nelson et al., 2005). Interactions between the nucleocapsid core and the cytoplasmic tail of E2 glycoprotein results in the budding of virus particles from the plasma membrane (Lee et al., 1996; Owen and Kuhn, 1997; Skoging et al., 1996). Though alphaviruses bud into icosahedral particles, the nucleocapsid core follows icosahedral symmetry only when it interacts with the ordered glycoprotein shell (Chmielewski et al., 2022; Lescar et al., 2001; Mangala Prasad et al., 2022; Mukhopadhyay et al., 2002a; Mukhopadhyay et al., 2002b; Pletnev et al., 2001). After virus exocytosis from host cell, E3 dissociates from the virion with only E1 and E2 forming the glycoprotein complex on mature virion (Holmes et al., 2020).

Although alphaviruses and flaviviruses differ in their cellular life cycles and respective glycoprotein arrangements on virion surface; both virus structures follow icosahedral symmetry, making the overall cryo-EM structure determination process similar for these virus genera. During the past few decades, cryo-EM structures of these viruses have

Table 1
Alphavirus structures with near-atomic resolution (<5.0 Å).

S. No.	Structure	EMD ID	Year	Resolution (Å)	Reference
1.	VEEV	EMD-5275	2011	4.8	(Zhang et al., 2011b)
2	VEEV VLP	EMD-31566	2021	3.5	(Ma et al., 2021)
3	VEEV VLP	EMD-24117	2021	4.2	(Basore et al., 2021)
4	VEEV VLP-LDLRAD3	EMD-24116	2021	4.3	(Basore et al., 2021)
5	VEEV VLP-LDLRAD3	EMD-31567	2021	3.0	(Ma et al., 2021)
6	VEEV VLP	EMD-25102	2022	4.2	(Kafai et al., 2022)
7	VEEV VLP- Fab hVEEV-63	EMD-25103	2022	4.0	(Kafai et al., 2022)
8	SINV	EMD-9693	2018	3.5	(Chen et al., 2018)
9	CHIKV-mouse Mxra8	EMD-9395	2019	5.0	(Basore et al., 2019)
10	CHIKV	EMD-5577	2013	5.0	(Sun et al., 2013)
11	CHIKV VLP	EMD-9393	2019	4.2	(Basore et al., 2019
12	CHIKV-Fab fragment of CHK-263	EMD-30477	2020	4.7	(Zhou et al., 2020b)
13	MAYV	EMD-22961	2021	4.4	(Ribeiro-Filho et al., 2021)
14	Barmah Forest virus (BFV)	EMD-1886	2011	5.0	(Kostyuchenko et al., 2011)
15	GETV	EMD-31533	2022	2.8	(Wang et al., 2022b)
16	GETV	EMD32412	2022	3.5	(Wang et al., 2022c)
17	EEEV VLP	EMD-22276	2020	4.2	(Williamson et al., 2020)
18	Chimeric EEEV	EMD-9280	2018	4.4	(Hasan et al., 2018b)

Table 2
Flavivirus structures with near-atomic resolution (<5.0 Å).

S. No.	Structure	EMD ID	Year	Resolution (Å)	Reference
1	Usutu virus (USUV)	EMD-23273	2021	2.4	(Khare et al., 2021)
2	TBEV	EMD-14512	2022	3.3	(Pulkkinen et al., 2022)
3	Mature TBEV	EMD-3752	2018	3.9	(Fuzik et al., 2018)
4	Mature TBEV-Fab-19/1786	EMD-3754	2018	3.9	(Fuzik et al., 2018)
5	DENV1	EMD-2142	2013	4.5	(Kostyuchenko et al., 2013)
6	DENV2	EMD-5520	2012	3.5	(Zhang et al., 2013b)
7	DENV2- scFv Fragment of EDE1 C10	EMD-30465	2021	3.5	(Sharma et al., 2021)
8	DENV2_NGC_Fab_C10 (28 °C)	EMD-31677	2021	3.1	(Lim et al., 2021)
9	DENV2_NGC_Fab_C10 (4 °C)	EMD-31680	2021	4.4	Lim et al., 2021)
10	DENV2- Fab SIgN-3C (pH 6.5)	EMD-30194	2020	4.2	(Zhang et al., 2020)
11	DENV2- Fab SIgN-3C (pH 8.0)	EMD-30195	2020	4.5	(Zhang et al., 2020)
12	DENV4	EMD-2485	2014	4.1	(Kostyuchenko et al., 2014)
13	Chimeric Binjari virus (BinJV) and DENV2	EMD-23042	2021	2.5	(Hardy et al., 2021)
14	WNVKUN	EMD-23044	2021	3.1	(Hardy et al., 2021)
15	Chimeric BinJV and KUNV	EMD-23043	2021	2.9	(Hardy et al., 2021)
16	Chimeric BinJV and Murray Valley Encephalitis Virus (MVEV)	EMD-23045	2021	3.7	(Hardy et al., 2021)
17	JEV	EMD-6685	2017	4.3	(Wang et al., 2017)
18	JEV-2F2 Fab complex	EMD-6854	2018	4.7	(Qiu et al., 2018)
19	Spondweni virus (SPOV)	EMD-11371	2021	2.6	(Renner et al., 2021a)
20	DENV2	EMD-11370	2021	3.1	(Renner et al., 2021a)
21	Immature BinJV	EMD-23147	2021	4.4	(Newton et al., 2021)
22	ZIKV	EMD-7543	2018	3.1	(Sevvana et al., 2018)
23	ZIKV	EMD-8116	2016	3.8	(Sirohi et al., 2016)
24	Thermally stable ZIKV	EMD-8139	2016	3.7	(Kostyuchenko et al., 2016)
25	ZIKV-E protein-ADI30056	EMD-22818	2020	4.0	(Sevvana et al., 2020)
26	ZIKV-Fab ZIKV-195	EMD-9131	2019	4.0	(Long et al., 2019)
27	ZIKV-Fab C10 at pH 6.5	EMD-9573	2016	4.4	(Zhang et al., 2016)
28	ZIKV-Fab C10 at pH 8.0	EMD-9575	2016	4.0	(Zhang et al., 2016)
29	ZIKV- Fab SIgN-3C (pH 6.5)	EMD-30192	2020	3.8	(Zhang et al., 2016
30	ZIKV- Fab SIgN-3C (pH 8.0)	EMD-30193	2020	4.8	(Zhang et al., 2016
31	ZIKV-Fab	EMD-30337	2020	4.1	(Tyagi et al., 2020)

progressed from low resolution (24–35 Å) (Fuller, 1987; Kuhn et al., 2002; Vogel et al., 1986) to near-atomic resolutions (2.4—2.8 Å) (Hardy et al., 2021; Khare et al., 2021; Wang et al., 2022a; Wang et al., 2022b) (Table 1 and 2). These studies have elucidated the structural features of these viruses and provided important insights into surface epitopes, receptor binding, fusion mechanism, assembly, and budding.

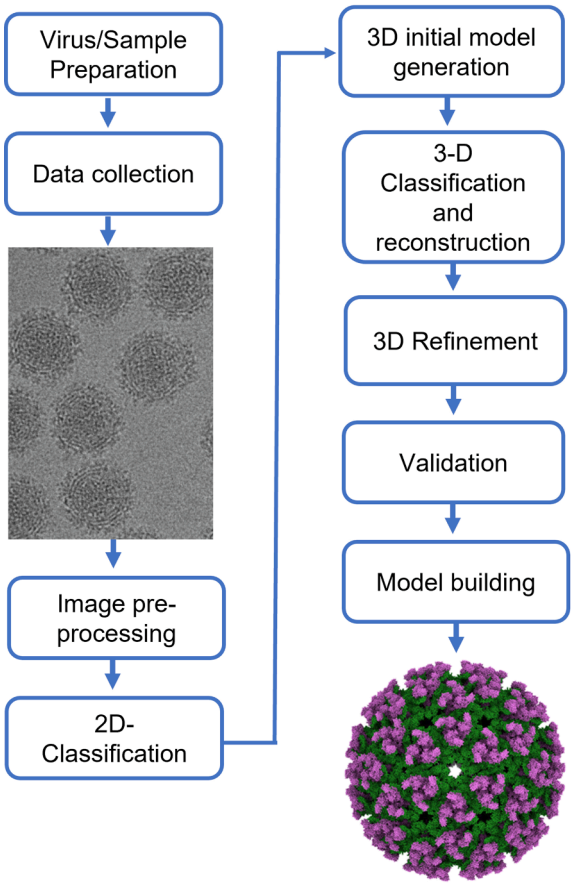

Fig. 2. General workflow of Single Particle Reconstruction.

2. Three-dimensional (3D) structural determination of flaviviruses and alphaviruses using single particle cryo-EM

Cryo-EM imaging produces two-dimensional (2D) projection images of 3D virus particles. Cryo-EM images collected across different areas on a sample grid, containing virus samples spread randomly, provide different views or projections of a given virus particle. These 2D projection images from different virions in the sample are then computationally combined to reconstruct a 3D electron density map of the virus using algorithms primarily based on the 'central section theorem' or projection slice theorem (Crowther et al., 1970a; De Rosier and Klug, 1968). The 'central section theorem' states that the Fourier transform (FT) of a 2D projection of a 3D object is identical to a central section of the FT of the 3D particle. This section passes through the origin in a perpendicular direction to the projection. Thus, the original 3D particle can be regained by using these many central sections to fill a volume in Fourier space and then calculating the inverse FT of this volume (Crowther and Amos, 1972; Rosenthal, 2015). A general overview of single-particle cryo-EM reconstruction is given in Fig. 2 and explained in the following sections.

With rapid advancements in microscope instrumentation, image processing algorithms, and computational methods, single particle 3-D reconstruction of alphaviruses and flaviviruses has now achieved near-atomic resolutions. The backbone models can be consistently built which allows residue-level understanding of viral architecture, assembly, and conformational changes between different viral states. Moreover, with advancements in asymmetric reconstruction strategies, it is now possible to visualize the complete virion structure with both its icosahedral and non-icosahedral structural features.

2.1. Cryo-EM sample preparation of alphaviruses and flaviviruses

Sample preparation is an essential part of cryo-EM experiments. A purified virus sample, either alone or in conjunction with other biomolecules, is applied onto glow-discharged TEM grids, blotted to a thin aqueous layer, and immediately plunge-frozen in liquid ethane (around −180 °C) (Dubochet et al., 1982b). Though viruses can be directly isolated from their natural reservoirs, such as pigs (Wang et al., 2022c), and mosquitoes (Fu et al., 2017; Mourya et al., 2001), the production of these viruses in large quantities suitable for structural analysis is carried out by infections in cultured cell lines (Fuller, 1987; Kuhn et al., 2002; Mangala Prasad et al., 2022; Prasad et al., 2017; Sirohi et al., 2016). Virus-like particles (VLPs) have also been designed for alphaviruses (Hohn et al., 2007) which replicate the original virus architecture but are non-infectious, making them safer for experimental handling (Basore et al., 2021; Sun et al., 2013; Yap et al., 2017). For flaviviruses, designing VLPs that faithfully represent the wild-type virions has not been successful, however recombinant subviral particles (RSPs) that consist only of prM and E glycoproteins without the capsid protein have been characterized which are smaller in diameter than the native virion (Allison et al., 2003; Chao et al., 2014; Ferlenghi et al., 2001).

Homogenous virus preparation is critical for obtaining near-atomic resolution cryo-EM reconstruction. This is a challenge, especially for flaviviruses, as viruses secreted from cells are generally a heterogeneous mixture of mature and partially mature virions due to inefficient prM cleavage by cellular furin protease. Thus, strategies to obtain homogenous mature flavivirus samples have been developed. One example is the use of Vero-furin cells which stably express high levels of human furin causing enhanced prM cleavage and resulting in a higher percentage of mature virions in flavivirus preparations (Mukherjee et al., 2016). Similarly, improved homogenous flavivirus preparations have also been obtained by creating chimeric viruses using prM-E proteins from pathogenic flaviviruses incorporated into an insect-specific flavivirus, namely, Binjari virus (BinJV), along with substitution of WNV (Kunjin strain) specific furin cleavage site into the target prM-E sequence. This approach has been successful in large scale production of homogenous and mature virion particles due to relatively high replication efficiency of the chimeric virus and improved furin cleavage enabling near-atomic resolution structure determination of mature flavivirus particles (Hardy et al., 2021). Nearly homogenous preparations of immature flavivirus, as secreted naturally in the case of BinJV, has also resulted in the highest resolution structure of immature flavivirus till-date (Newton et al., 2021).

2.2. Microscope setup and data collection

Developments in the transmission electron microscope (TEM) and detector hardware have been critical in the evolution of the single-particle analysis (SPA) methodology. For example, commercial stable cold stages allowed imaging of samples at liquid nitrogen temperature (Vogel et al., 1986). Image quality also improved with brighter and more coherent electron beams producing field emission guns (Suloway et al., 2005). Initially, EM images were recorded on film, which required development and digitization (Mancini et al., 2000; Sun et al., 2013). Subsequently, CCD cameras came into existence that allowed automation of data collection and resulted in near-atomic resolution structures of flavivirus (Bammes et al., 2011; Zhang et al., 2013b) and alphavirus (Zhang et al., 2011a). However, due to the indirect detection of electrons, CCD images suffered from loss of resolution and sensitivity. Major improvements in the resolution of single particle cryo-EM structures are owed mainly to the advent of direct electron detectors (DED) (McMullan et al., 2009). Images from a DED have higher contrast, preserve high-resolution signal at low electron doses, and have faster readouts, enabling the recording of multi-frame images or movies. Simultaneous improvement in data collection software such as Leginon (Carragher et al., 2000), SerialEM (Mastronarde, 2005), EPU (ThermoFisherScientific), Latitude S (Gatan, Inc.) and UCSFImage (Li et al., 2015) has also made large scale data collection user-friendly. These advancements in detector and data collection throughput have significantly contributed to achieving high-resolution structures for alphaviruses (Chen et al., 2018; Wang et al., 2022b; Wang et al., 2022c) and flaviviruses (Hardy et al., 2021; Sevvana et al., 2018) by improving data quality and quantity.

2.3. Image processing workflow

Single-particle cryo-EM data is collected in the form of either images or movies. The raw cryo-EM images can be blurred, have a low signal-to-noise ratio (SNR), or have other issues such as astigmatism, which needs to be corrected or accounted for to extract the highest signal information.

2.3.1. Motion correction

Traditional detectors, such as film and CCD cameras, often output blurry images because of beam-induced particle movement during image acquisition, which reduces data quality (Henderson and Glaeser, 1985). Using DEDs, images can now be collected as a movie or a series of frames at short-time exposure. Cross-correlation between frames within one exposure can efficiently correct the uniform whole-frame motion. This algorithm has been incorporated in MotionCorr (Li et al., 2013) software which was successfully employed in near-atomic resolution structure determination of flaviviruses (Kostyuchenko et al., 2016; Wang et al., 2017) and alphaviruses (Zhou et al., 2020b). More recent beam-induced motion correction algorithms such as MotionCorr2 (Zheng et al., 2017) assume the sample motion as a local distortion that changes smoothly during the exposure and it corrects both uniform whole-frame motion plus anisotropic local motion. Examples, where MotionCorr2 has been used for frame alignment, include mature and immature Kunjin virus (KUNV) (Therkelsen et al., 2018) (flavivirus), DENV (Hardy et al., 2021) (flavivirus), and VEEV (Ma et al., 2021) (alphavirus) structures. The subsequently de-blurred image is used for defocus and contrast transfer function determination. Movie alignment of frames using the Imagic-4D software package was used for MAYV (alphavirus) cryo-EM data processing (Ribeiro-Filho et al., 2021).

2.3.2. CTF estimation

Cryo-EM images recorded in a TEM are affected by the microscope parameters and can be defined by its contrast transfer function (CTF). The CTF is a function of many terms, such as electron wavelength (defined by the accelerating voltage of the microscope), the spherical aberration of the microscope lens, and the applied under-focusing (or defocusing) of the image. Only the defocus of images varies in a typical cryo-EM dataset while other terms affecting CTF are constant for a given data collection session. Thus, the defocus for each motion-corrected average image is determined by fitting a CTF model to the observed CTF. CTF correction can then be performed to restore the correct phases at all spatial frequencies in an image. Several programs can automatically or semi-automatically compute these CTF parameters, such as Gctf (Zhang, 2016), CTFFIND (Mindell and Grigorieff, 2003), and CTFIT in EMAN (Ludtke et al., 1999). Examples, where Gctf has been used for CTF determination, include SINV/EEEV alphavirus (Williamson et al., 2020) and many flaviviruses reconstructions (Fuzik et al., 2018; Hardy et al., 2021; Newton et al., 2021; Wang et al., 2017; Williamson et al., 2020). Similarly, CTFFIND4 was used for CTF determination of several alphaviruses (Chen et al., 2022; Chen et al., 2018; Hasan et al., 2018c; Ma et al., 2021; Mangala Prasad et al., 2022; Wang et al., 2022b) and flaviviruses (Pulkkinen et al., 2022; Renner et al., 2021b; Sevvana et al., 2018; Therkelsen et al., 2018) resulting in high-resolution structures. CTFIT (EMAN) has also been used for CTF correction of both flavivirus (Zhang et al., 2013b) and alphavirus (Sun et al., 2013; Zhang et al., 2011a) cryo-EM reconstructions. Recently, the Imagic program CTFFIND was used for full-dataset CTF correction of MAYV (alphavirus)

(Ribeiro-Filho et al., 2021). For thick samples, defocus variation can also occur along the ice thickness which further affects accurate signal assessment. Thus, defocus gradients are also taken into account during the reconstruction process, such as in the case of GETV cryo-EM reconstruction (Wang et al., 2022b; Zhu et al., 2018).

2.3.3. Particle selection and extraction

The next step of image processing is individual particle identification and extraction from cryo-EM micrographs. As alpha- and flavivirions are large spherical entities, they do not require extensive particle-picking strategies as may be required for smaller asymmetric protein complexes. Manual, automated, and semi-automated detection approaches have been used for virus particle picking. Visualization of selected particles by the human eye is essential for manual picking and can be improved by using low-pass filters. For example, e2boxer (EMAN2) (Tang et al., 2007) has been used for boxing and manual particle picking of immature ZIKV (flavivirus) (Newton et al., 2021; Prasad et al., 2017) and CHIKV-MXRA8 (alphavirus) (Song et al., 2019). Whereas, Newton et al. used Relion (Scheres, 2012) for manual particle picking of BinJV (flavivirus). In the semi-automated process, a subset of particles is manually picked from a few representative micrographs that cover the defocus range of the dataset and are used to calculate low-resolution 2D class averages. These 2D classes are used as templates for automated particle picking from the entire dataset. For example, Xmipp (Scheres et al., 2008) has been used for semiautomatic particle picking of TBEV (flavivirus) (Pulkkinen et al., 2022). Using a gaussian blob of a defined range of radius is another standard particle-picking method (Zivanov et al., 2018). The picked particles are then extracted from the micrographs to create a particle stack. Single particle analysis software such as EMAN2, Relion, and Xmipp have primarily been used for automatic as well as manual particle picking and extracting particles (Scheres, 2012; Scheres et al., 2008; Tang et al., 2007). For instance, Chen et al. used eboxer2.py from EMAN2 for particle picking of SINV (alphavirus) (Chen et al., 2018) while automatic particle picking of VEEV VLP-LDLRAD3-D1 complex particles (alphavirus) was performed using the Laplacian-of-Gaussian model available in Relion (Ma et al., 2021).

Other programs used for particle picking of flaviviruses; include FindEM (Roseman, 2004) which was used for mature and immature KUNV datasets (Therkelsen et al., 2018), cryoSPARC (Punjani et al., 2017) in case of Spondweni virus (SPOV) particles and Ethan (Kivioja et al., 2000) for DENV (Renner et al., 2021a; Zhang et al., 2013b).

2.3.4. 2D classification

At this stage, stacks of extracted virus particle images are available free of drift, and CTF estimated. The next step is increasing the SNR by sorting, aligning, and averaging 2D images according to their in-plane rotations and translations. This procedure is known as 2D classification or 2D averaging. 2D averaging is vital for producing high-quality initial 3D models and dumping bad particles (Chung et al., 2020). Unsupervised or reference-free alignment is carried out to group particles by statistically comparing all particle images pixel by pixel using principal component or multivariate statistical analysis. Another approach is by using maximum likelihood (ML) which allocates a specific particle to a set of classes with a probability distribution (Sigworth, 1998). Based on maximum interclass and minimum intraclass variance, particles are grouped into 2D classes which can then be iteratively refined to reduce variations within the classes. Thus, each 2D class represents a specific view of the stoichiometrically and conformationally homogeneous particle images and shows greater details because of its enhanced signal-to-noise ratios compared to original images (Frank, 1990; Van Heel et al., 2000).

2D class averaging provides valuable awareness of a dataset's heterogeneity and orientation bias. The high structural symmetry applicable to alpha- and flavivirions generally produces a compact set of classes. The 'bad classes' which are generally identified by their lack of well-resolved features, can be discarded at this stage, and iterative 2D classification steps can be done to refine the quality of classes. Only the refined, high-quality 2D classes are then used for 3D classification and reconstruction. Data processing software packages are available that can perform alignment and 2D classification with different degrees of manual control. For example, Scipion (de la Rosa-Trevín et al., 2016; Lander et al., 2009), Appion (Lander et al., 2009), EMAN (Ludtke et al., 1999), Relion (Scheres, 2012) and cryoSPARC (Punjani et al., 2017). Relion has been employed for reference-free 2D class averaging of many flaviviruses (Newton et al., 2021; Prasad et al., 2017; Pulkkinen et al., 2022; Sevvana et al., 2018) and alphaviruses (Chen et al., 2018; Mangala Prasad et al., 2022; Wang et al., 2022b).

3. 3D reconstruction: Obtaining 3D information from 2D projections

After having 2D class averages with improved SNR, the next step is 3D reconstruction. All 3D reconstruction methods follow a general path of initial 3D model generation, relative five spatial orientation determination, and 3-D map synthesis. The differences lie in the algorithms used for alignment and reconstruction.

3.1. Initial 3D model generation

The first step common to all the 3D reconstruction methods is to generate an initial 3D reference model. An initial model can be built by determining the common lines of a few images and computing their icosahedral orientations without using any reference model (Crowther et al., 1970a)(). The common lines method was used for the reconstruction of SFV (Fuller, 1987) and DENV (Kuhn et al., 2002). For small icosahedral virions like alpha- and flaviviruses even a soft sphere can be used as an initial model (Mangala Prasad et al., 2022). Alternatively, a low-resolution initial 3D model can also be generated *ab initio* by randomly allocating icosahedral orientations to a few hundred 2D class averages and reconstructing a 3D density of approximately the size of the target virus particle (Liu et al., 2007). This method is known as the Multipath simulated annealing approach (MPSA) and has been used for center and orientation determination of both flaviviruses (Kostyuchenko et al., 2014; Kostyuchenko et al., 2013; Zhang et al., 2013b) and alphaviruses (Zhang et al., 2011a). Furthermore, a previously determined icosahedral alphavirus (Song et al., 2019; Wang et al., 2022c; Williamson et al., 2020) or flavivirus density map can be used to generate an initial model by scaling its size to match the experimental dataset, and subsequently, low pass filtering the density map to only retain the overall shape and size of the virion (Hardy et al., 2021; Renner et al., 2021a).

3.2. Orientation determination

SPA's most challenging and rate-limiting step is particle orientation and center determination. This process primarily involves correlating the virus particle images with 2D reference projections from an initial 3D model or a model obtained in the previous iteration and determining orientation and particle center.

3.2.1. Common lines method

Ab initio 3D reconstructions can be obtained computationally by computing the relative orientation between particles using the common line theorem that says that each pair of 2D projections of the same 3D structure has at least one line (1D) projection in common. In Fourier space, a common line is the intersection of FT of 2D projection planes that pass through the origin of the 3D FT of the object. Therefore, at least three 2D projections are needed for relative orientation determination. However, common lines using individual, noisy images produce unreliable 3D reconstructions. The presence of 2D class averaging and symmetry greatly helps the reconstruction (Crowther et al., 1970a; Crowther et al., 1970b). The common lines procedure has been

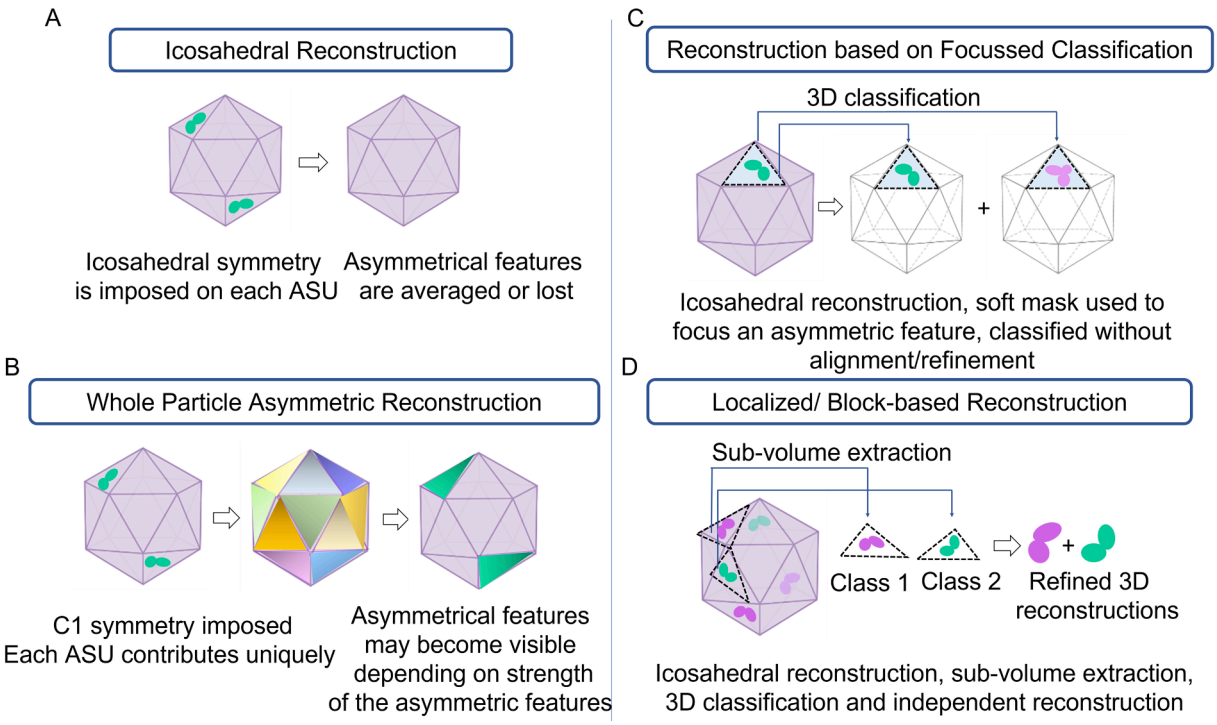

Fig. 3. Advanced 3D reconstruction methods for alphavirus and flaviviruses: (A) Icosahedral reconstruction; (B) Whole particle asymmetric reconstruction; (C) Reconstruction based on focused classification; (D) Localized or block-based reconstructions. Figures were created using BioRender.com.

employed for 3D reconstruction of alphaviruses such as SFV at 22 Å (Fuller et al., 1995) and 9 Å (Mancini et al., 2000) and SINV at 11 Å (Zhang et al., 2002), as well as flaviviruses such as DENV2 at 24 Å (Kuhn et al., 2002). This method is available in many software packages for example, EMAN2 (Tang et al., 2007), SIMPL (Elmlund and Elmlund, 2012), and real space IMAGIC (van Heel et al., 1996).

Another common lines-based algorithm for *ab initio* angular assignment in real space is angular reconstitution. The angular reconstitution algorithm assumes that particles are distributed with random orientations and sees intersecting 1-D lines from 2-D projections. Initially, 2-D class averages are chosen as starting points, preferably representing orthogonal views of the 3-D object. Random Euler angles are assigned to each class averages (statements) using sinograms, and sinogram functions to generate a preliminary 3D reconstruction . Then, reprojections of this initial 3D reconstruction are used as an anchor set for the next cycle of angular reconstitution (Schatz et al., 1997; Van Heel, 1987b). This process is repeated until convergence, followed by 3D reconstruction based on these angles employing a weighted-projection algorithm (Harauz and van Heel, 1986). Angular reconstitution has recently been used for orientation determination of MAYV particle datasets, resulting in a 4.4 Å resolution structure (Ribeiro-Filho et al., 2021).

3.2.2. *Projection matching (PM)*

In this method, pre-centered experimental 2D particle images are compared with computationally generated 2D views of a 3D reference model. Angles are assigned based on similarity functions such as cross-correlation, phase residuals, and overlap integral principles (Frank, 1990; Saxton and Frank, 1976; Van Heel, 1987a). The best-matched projection is allocated to each particle, assuming it to be true. After relative orientations are defined, each particle image is back-projected into a new 3D reconstruction. Projection matching has been used for orientation determination in many alphavirus reconstructions, such as VEEV (Zhang et al., 2011a), SINV (Zhang et al., 2002), CHIKV VLP (Sun et al., 2013) and EEEV (Hasan et al., 2018b) as well as flavivirus reconstructions such as DENV (Kuhn et al., 2002) (Pokidysheva et al., 2006) and WNV (Mukhopadhyay et al., 2003).

3.2.3. *Maximum Likelihood (ML)*

A more recent approach to orientation determination using a reference model is based on applying a maximum likelihood estimate to projection matching. Similar to 2D classification, ML-based orientation determination does not allocate a similarity-based single relative orientation to the particle image but rather assigns a set of probabilities to images in different orientations. ML methods can powerfully model the noise in cryo-EM images and automate judgments regarding filtering and weighting. Moreover, ML methods can identify coexisting heterogeneous structural states in the sample, delivering valuable insights into the viral life cycle (Scheres et al., 2005a; Scheres et al., 2005b; Sigworth, 1998). Many recent SPA reconstruction packages such as Relion, Frealign (Grigorieff, 2016), Xmipp, and PRIME (Elmlund et al., 2013) implement ML-based orientation determination. Besides, Relion also incorporates an ML-based ability to classify heterogeneous samples. Among the SPA of flaviviruses and alphaviruses, ML-based methods have helped achieve resolution better than 3 Å (Hardy et al., 2021; Khare et al., 2021; Ma et al., 2021; Renner et al., 2021a; Sevvana et al., 2018; Wang et al., 2022b).

3.3. *3D refinement*

Once each particle is assigned its orientations and a 3D map is reconstructed, it can be further refined by iterative cycles of projection matching with finer angle search. Each new cycle improves the accuracy of orientations, and more accurate angles will produce higher-resolution maps. After several iterations, the reconstruction process reaches a point where no significant changes in orientation assignments occur, and a final 3D map is thus generated (Guo and Jiang, 2014b). Various 3D cryo-EM map refinement software are available such as CryoSPARC, Relion, and Phenix (Afonine et al., 2018) which employ a combination of statistical methods like Bayesian inference and maximum-likelihood optimization to refine the maps.

3.3.1. *High-resolution refinement/polishing*

The second phase of refinement or polishing is carried out to further

improve the 3-D map quality. Only the good particles with predetermined orientation/center parameters from the first refinement phase are used to further refine the orientations to sub-degree and centers to subpixel accuracy (Guo and Jiang, 2014a; Guo and Jiang, 2014b). Furthermore, additional parameters such as astigmatism, defocus, CTF, beam tilt, and magnification/elliptical distortion are also refined in each iteration resulting in an improved 3D map resolution (Guo and Jiang, 2014b; Sun et al., 2021). Another refinement approach is based on Bayesian analysis (Scheres, 2012) that has also been successful in improving the resolution of flavivirus cryo-EM structures such as in the case of SPOV, DENV (Renner et al., 2021a), and TBEV (Pulkkinen et al., 2022).

4. 3D classification and sub-icosahedral reconstruction

Icosahedral structure redundancy has been advantageous to structural biology to gain resolution by averaging different subunits together. Although alphaviruses and flaviviruses are icosahedral viruses having highly symmetrical envelope and capsid characteristics, inherent asymmetric elements also exist such as the genomic RNA and minor structural proteins which do not follow icosahedral symmetry. Applying icosahedral symmetry during 3D reconstructions of these virions results in asymmetrical features being obliterated or poorly resolved (Kostyuchenko et al., 2016; Sirohi et al., 2016; Therkelsen et al., 2018) (Fig. 3**A**). Additionally, there can be structural variability and compositional heterogeneity within the icosahedral arrangement of the virion shells themselves which can limit the resolution of the obtained structures. Analysis of local heterogeneity requires classifying particle images into structurally homogenous classes and can be performed using multiple 3D reference models for projection-matching. However, the lack of prior information on structural variability severely limits the pertinency of this approach (Nogales and Scheres, 2015). Development of an ML-based 3D classification approach (Scheres et al., 2007) has capitalized on this idea and has been used for the 3D classification of many alphaviruses (Chen et al., 2022; Song et al., 2019; Wang et al., 2022b) and flaviviruses (Fuzik et al., 2018; Therkelsen et al., 2018; Wang et al., 2017) to tease out minor inconsistencies and improve the overall resolution of the cryo-EM structures. In addition, recent strategies of localized and sub-particle reconstructions have helped to resolve local heterogeneities in virus structures and further improve map resolutions. Below we discuss non-icosahedral methods used for the alphavirus and flavivirus 3D reconstructions.

4.1. Whole particle asymmetric refinement

The simplest way to resolve asymmetry is excluding symmetry constraints while averaging the dataset, also called C1 symmetry reconstruction. The process is computationally expensive for it samples the complete globe of probable orientations (Fig. 3**B**) This method also compromises the resolution as each icosahedral particle contributes to the final reconstruction only once for every symmetry-related orientation. This strategy has been used to resolve the variable position of the flavivirus nucleocapsid concerning the outer glycoprotein layer in KUNV and ZIKV (Therkelsen et al., 2018).

4.2. Reconstructions based on focused classification

The computational search of particle orientations is limited to a single asymmetric unit (ASU) during an icosahedral refinement (Scheres, 2012). Thus, each ASU contributes equally to the 3D reconstruction regardless of having asymmetric features in some areas of the structure. Symmetry expansion is performed to mine out unique asymmetric elements that involve the assignment of every possible symmetry-based orientation to each particle and the alignment of each ASU in the dataset. Symmetry expansion is subsequently followed by either focused classification or localized or block-based reconstruction depending upon the type of structural heterogeneity (Discrete vs. continuous heterogeneity) (Goetschius et al., 2019). For example, discrete heterogeneities such as partial occupancy of Fab fragments on the E glycoproteins can be quantified using focused classification (Ilca et al., 2015). Focussed classification uses a mask to identify a smaller sub-volume (suspected to have unique features) within the refined virus structure and the masked volume is then subjected to 3D classification without the further refinement of angles or offsets (Fig. 3**C**). Focussed classification has been successfully applied to the reconstruction map of the TBEV flavivirion complexed to a Fab fragment to delineate virus population classes representing occupied and unoccupied Fab sites (Fuzik et al., 2018).

4.3. Localized/Block-based reconstruction

Whereas focussed approaches use a mask to define the sub-volume of interest, sub-particle reconstruction methods extract smaller sub-particle volumes from the full virion particles. The extracted sub-volumes are re-centered, re-extracted from the original micrographs, and 3D classified which allows for precise offsets and angular refinements (Fig. 3**D**). To improve the low-resolution icosahedral maps of alphavirus EEEV at low pH, local reconstruction of ASU which contained glycoprotein spikes from both quasi-3-fold and icosahedral 3-fold symmetry positions was performed (Chen et al., 2022). Sixty ASU from each particle image in the dataset was extracted using the localrec program (Ilca et al., 2015) and reconstructed using cisTEM (Grant et al., 2018). Improved resolution in each case demonstrated that EEEV particles experience conformational changes causing spatial dislocations of E1-E2 glycoproteins in each ASU and indicating an imperfect icosahedral symmetry on the viral surface (Chen et al., 2022). DilNunno et al. extracted a raft subvolume (containing three M and E dimer pairs) from ZIKV (flavivirus) 3D map using their in-house ISECC software and followed it up with 3D classification and reconstruction of the sub-volumes using Relion. Local reconstruction improved the resolution to 3.4 Å and led to the discovery of two previously undiscovered lipid moieties located near M and E helices (DiNunno et al., 2020). Likewise, Renner et al. obtained a 3.8 Å resolution map by local reconstruction of glycoprotein spikes in immature SPOV (flavivirus) (Renner et al., 2021a).

A similar sub-particle approach involves partitioning the virion structure into smaller blocks (which may not be the ASU) after conventional icosahedral refinement. Subsequently, the 2D image of each block is re-extracted, classified, and refined (reconstructed) independently with its local mean defocus value (Zhu et al., 2018) (Fig. 3**D**). Finally, reconstructions of all blocks are combined to produce a complete virion structure. This block-based procedure was successfully employed to improve resolution, resolve structural plasticity and defocus gradient in the ~ 70 nm GETV alphavirion. Three categories of blocks comprising two trimers near the icosahedral twofold axis, four trimers near the icosahedral-three-fold axis, and five trimers near the icosahedral fivefold axis were extracted from a 4.1 Å map, 3D classified and refined independently, followed by local defocus estimation. Final 3D refinement yielded 2.85 Å, 2.92 Å, and 2.81 Å density maps respectively for the different blocks (Wang et al., 2022b). Likewise, resolution damage caused due to the plasticity of the virus has been compensated by block-based reconstruction. The icosahedral reconstruction of VEEV VLP (alphavirus) in complex with its receptor LDLRAD3-D1 at 4.1 Å resolution was improved by extracting two blocks (one block of five trimer spikes plus linked capsid near the five-fold axis and the second block contains six trimers plus capsid around the two-fold axis) and reconstructing them separately. The final refinements resulted in a 3.0 Å (five-fold block) and 3.1 Å maps (two-fold block). The resulting structure showed detailed contacts between the LDLRAD3 receptor protein and the VEEV glycoproteins (Ma et al., 2021). A similar methodology was also used to solve the structure of another alphavirus, SINV, to 3.5 Å (Chen et al., 2018).

5. Resolution evaluation and validation of cryo-EM maps

The next step in SPA involves validation of the accuracy of 3D reconstruction results. Most reconstruction algorithms use a "gold-standard" technique where datasets are divided into two halves at the outset and processed independently. The resulting half-reconstruction maps are cross-correlated as a spatial frequency function to determine the resolution. These correlations are called "Fourier Shell Correlations (FSCs)". The 0.143 threshold is used as a criterion for determining the final resolution of the reconstruction map. The resolution obtained from completely independent reconstruction will be free of model bias and accurate (Harauz and van Heel, 1986; Scheres and Chen, 2012). Another method is tilt pair validation which involves the consistency test between the orientation of the tilted particle whose tilt angle and tilt axis are known and the untilted particle whose orientation is determined in the model reconstruction (Henderson et al., 2011). Further, the quality of density maps can be evaluated visually at various resolutions. For example, protein backbone and side chains can be modeled faithfully at ~ 2 Å and most side chains can be defined near 3 Å. At 4 Å, protein backbone tracing and bulky side chains can be located as the pitch of alpha helices and separate beta strands are intact. However, at 5–8 Å, protein backbone tracing is ambiguous with loss in the separation of beta-strands and alpha-helices visible as only rod-shaped densities. Beyond 8 Å, only rigid-body model fitting can be done as the resolution is insufficient for secondary structure modeling (Baker et al., 2007). For symmetrical viruses, validation at low resolution can also be achieved through the triangulation number and copy number spotted from the reconstruction which is known for alpha- and flaviviruses (Guo and Jiang, 2014b).

High-resolution density contrast in a cryo-EM map is critical for structure interpretation which is lost due to resolution-dependent amplitude or B-factor falloff. This B-factor is restored by plotting the logarithm of radially averaged amplitude against the square of reciprocal resolution and fitting it to a linear decay function in the Guinier plot. The estimated B-factor is then applied to the resolution shells to restore the amplitude through a process called map sharpening. (Rosenthal and Henderson, 2003). Map sharpening does not affect resolution but improves interpretability which in turn helps to build better atomic models in the cryo-EM map. The built atomic model evaluation can be carried out using software such as Coot (Emsley and Cowtan, 2004), Buccaneer (Cowtan, 2006), wARP/ARP (Pereira and Lamzin, 2017), or PHENIX (Afonine et al., 2018). The final quality of the model can also be evaluated using software like MolProbity (Chen et al., 2010) and PROCHECK (Laskowski et al., 1993), which evaluate stereochemistry parameters of the atomic model (bond length, angles, and Ramachandran plot).

6. Discussion/ conclusion

The past few decades have seen many sub-nanometer resolution (6–10 Å) (Mancini et al., 2000; Prasad et al., 2017; Song et al., 2019; Therkelsen et al., 2018; Williamson et al., 2020; Zhang et al., 2003a) and several near-atomic resolution (2–4 Å) (Chen et al., 2018; Hardy et al., 2021; Khare et al., 2021; Ma et al., 2021; Renner et al., 2021a; Sevvana et al., 2018; Wang et al., 2022a; Zhang et al., 2013b) reconstructions of alphavirus and flavivirus structures. Both cryo-electron microscope instrumentation and image processing advances have been major contributors to this increase in structure resolutions. Notable technical breakthroughs essential for the success of the SPA methodology have been the commercial cold stages, field emission gun, intermediate voltage, and improved illumination systems, DED detection, and the automation of data collection (Barton et al., 2011; McMullan et al., 2009; Suloway et al., 2005). Equally significant has been the development of robust algorithms for various steps in SPA workflow in the last few decades (Frank et al., 1996; Grigorieff, 2007; Punjani et al., 2017; Scheres, 2012; Scheres et al., 2008; Tang et al., 2007; van Heel et al., 1996).

Table 3
High resolution Cryo-EM structures of neutralization antibodies complexed with alphaviruses (<10 Å).

S. No.	Structure	EMD ID	Year	Resolution (Å)	Reference
1.	EEEV-3	EMD-9274	2018	7.3	(Hasan et al., 2018b)
2	EEEV-5	EMD-9275	2018	7.5	(Hasan et al., 2018b)
3	EEEV-42	EMD-9249	2018	7.7	(Hasan et al., 2018b)
4	EEEV-58	EMD-9278	2018	7.3	(Hasan et al., 2018b)
5	EEEV-Fab22 (pH 7.4)	EMD-24203	2022	6.7	(Chen et al., 2022)
6	Chimeric SINV/EEEV-IgG-94	EMD-26946	2023	6.6	(Williamson et al., 2023)
7	Chimeric SINV/EEEV-IgG-106	EMD-26947	2023	5.2	(Williamson et al., 2023)
8	Chimeric EEEV-33	EMD-22223	2021	7.2	(Williamson et al., 2023)
9	CHK-124	EMD-30476	2020	5.2	(Zhou et al., 2020a)
10	CHK-263	EMD-30477	2020	4.7	(Zhou et al., 2020a)
11	CHK-263 IgG	EMD-30478	2020	5.9	(Zhou et al., 2020a)
12	Fab chk-265	EMD-21509	2020	5.3	(Powell et al., 2020)
13	RRV-Fab chk-265	EMD-21473	2020	6.3	(Powell et al., 2020)
14	hVEEV-63	EMD-25103	2022	4.0	(Kafai et al., 2022)
15	VEEV VLP- Fab hVEEV-63	EMD-25103	2022	4.0	(Kafai et al., 2022)

Due to the availability of high-resolution cryo-EM structures, novel structural insights into these viruses' architecture, assembly, disassembly and maturation have been possible. Among flaviviruses, high resolution structures have revealed distinct lipid moieties that lie in binding pockets formed by transmembrane helices of E and M proteins (DiNunno et al., 2020) (Hardy et al., 2021) (Renner et al., 2021a). These lipid binding pockets have been proposed to stabilize the E protein on mature virions and identified as potential target for antiviral development. Similar hydrophobic binding pocket has also been identified in alphaviruses (Chen et al., 2018). In case of alphaviruses, previously undescribed glycosylation and S-acylation sites in both the E1 and E2 glycoproteins have also been identified that might be involved in viral immune evasion, cell-entry, and stabilizing the E1-E2 heterodimer in the lipid bilayer (Wang et al., 2022b; Wang et al., 2022c). Whole particle asymmetric refinement of the immature and mature flavivirus have shown the variations in nucleocapsid core interactions with surface glycoproteins (Therkelsen et al., 2018). Similarly, high resolution structure of immature flaviviruses (Kostyuchenko et al., 2013; Newton et al., 2021; Renner et al., 2021a); has provided detailed insights into the furin recognition site on prM protein and mechanism of flavivirus maturation. High resolution cryo-EM structures of alphaviruses have also contributed to our understanding of virus maturation and processing of glycoproteins to produce infectious virions (Yap et al., 2017).

Cryo-EM structures of both alphaviruses and flaviviruses in complex with various receptors (such as VEEV vlp-LDLRAD3 (Basore et al., 2021; Ma et al., 2021), CHIKV-Mxr8 (Basore et al., 2019), EEEV-Heparan sulfate analogue (Chen et al., 2020), and DENV-DC-SIGN carbohydrate recognition domain (Pokidysheva et al., 2006)) have been reported which have elucidated epitopes involved in virion entry into the host cell. Additionally, cryo-EM structures have provided insights into conformational intermediates and alternate structural states for alpha- and flaviviruses during their life cycles (Chen et al., 2022; Fibriansah et al., 2013; Morrone et al., 2020a; Morrone et al., 2020b; Yu et al.,

Table 4
High resolution Cryo-EM structures of neutralization antibodies complexed with flaviviruses (<10 Å).

S. No.	Structure	EMD ID	Year	Resolution (Å)	Reference
1	DENV2- scFv Fragment of EDE1 C10	EMD-30465	2021	3.5	(Sharma et al., 2021)
2	DENV2_NGC_Fab_C10 (28 °C) (1Fab:3E)	EMD-31677	2021	3.1	(Lim et al., 2021)
3	DENV2_NGC_Fab_C10 (28 °C) (2Fab:3E)	EMD-31678	2021	3.3	(Lim et al., 2021)
4	DENV2_NGC_Fab_C10 (28 °C) (3Fab:3E)	EMD-31679	2021	3.6	(Lim et al., 2021)
5	DENV2_NGC_Fab_C10 (4 °C)	EMD-31680	2021	4.4	(Lim et al., 2021)
6	DENV2_F(ab')2-local	EMD-31681	2021	4.9	(Lim et al., 2021)
7	DENV2_NGC_F(ab')2	EMD-31682	2021	3.4	(Lim et al., 2021)
8	DENV2- Fab SIgN-3C (pH 6.5)	EMD-30194	2020	4.2	(Zhang et al., 2020)
9	DENV2- Fab SIgN-3C (pH 8.0)	EMD-30195	2020	4.5	(Zhang et al., 2020)
10	DENV2- Fab SIgN-3C (pH 5.0)	EMD-30196	2020	7.8	(Zhang et al., 2020)
11	DENV2- SIgN-3C IgG	EMD-30197	2020	6.1	(Zhang et al., 2020)
12	DENV2-anti-PrM12	EMD-29020	2023	10.2	(A. Dowd et al., 2023)
13	DENV2-anti-PrM13	EMD-29021	2023	9.8	(A. Dowd et al., 2023)
14	DENV2-human Fab 2D22	EMD-2967	2015	6.5	(Fibriansah et al., 2015)
15	DENV2-human Fab 2D22 (37 °C)	EMD-2996	2015	6.9	(Fibriansah et al., 2015)
16	DENV3-Fab 5J7	EMD-5935	2015	9.0	(Fibriansah et al., 2015)
17	DENV1-Fab 1F4	EMD-2442	2014	6.0	(Fibriansah et al., 2014)
18	JEV-2F2 Fab	EMD-6854	2018	4.7	(Qiu et al., 2018)
19	JEV-2H4 Fab	EMD-6855	2018	4.6	(Qiu et al., 2018)
20	TBEV-Fab 19/1786	EMD-3754	2018	3.9	(Fuzik et al., 2018)
21	ZIKV- Fab_G9E	EMD-33718	2023	5.9	(Adams et al., 2023)
22	ZIKV- DH1017.IgM Fabc	EMD-25606	2022	5.3	(Singh et al., 2022)
23	ZIKV-E protein-ADI30056	EMD-22818	2020	4.0	(Sevvana et al., 2020)
24	ZIKV-Fab	EMD-7613	2018	9.7	(Tharakaraman et al., 2018)
25	ZIKV-Fab C10	EMD-30279	2020	9.4	(Morrone et al., 2020a)
26	ZIKV-Fab	EMD-30337	2020	4.1	(Tyagi et al., 2020)
27	ZIKV-E protein-ADI30056	EMD-22818	2020	4.0	(Sevvana et al., 2020)
28	ZIKV-Fab ZIKV-195	EMD-9131	2019	4.0	(Long et al., 2019)
29	ZIKV-Fab C10 at pH 6.5	EMD-9573	2016	4.4	(Zhang et al., 2016)
30	ZIKV-Fab C10 at pH 8.0	EMD-9575	2016	4.0	(Zhang et al., 2016)
31	ZIKV- Fab SIgN-3C (pH 6.5)	EMD-30192	2020	3.8	(Zhang et al., 2020)
32	ZIKV- Fab SIgN-3C (pH 8.0)	EMD-30193	2020	4.8	(Zhang et al., 2020)
33	Immature ZIKV-DV62.5 Fab	EMD-0932	2020	8.0	(Tan et al., 2020)
34	ZIKV-Z23-Fab	EMD-9542	2016	9.4	(Wang et al., 2016)
35	BinJV-pr specific Fab 2A7	EMD-23330	2021	9.6	(Newton et al., 2021)

2008; Zhang et al., 2013a). Moreover, cryo-EM structures of neutralizing antibodies with these virions have revealed mechanistic insights into antibody interactions and highlighted protective surface epitopes pertinent to vaccine design (Table 3 & 4).

Within the group of known enveloped viruses, alpha- and flaviviruses have the largest repertoire of full virion structures solved by single particle cryo-EM. Cryo-EM reconstructions of other symmetrical enveloped viruses such as PBCV (3.5 A) Fang et al., 2019) and Rift Valley fever virus (13 Å) (Halldorsson et al., 2018) have been reported, but they are few in comparison. Furthermore, many enveloped viruses are pleomorphic which make them unsuitable for structure determination using SPA. The structural organization of these pleomorphic viruses has been determined using cryo-electron tomography (cryo-ET) and sub-tomogram averaging (STA) (Stass et al., 2019) such as in case of human immunodeficiency virus (Mangala Prasad et al., 2022; Mattei et al., 2016; Qu et al., 2021), influenza A virus (Harris et al., 2006; Huang et al., 2022; Peukes et al., 2020), ebola virus (Bharat et al., 2012; Tran et al., 2014; Wan et al., 2020) and severe acute respiratory syndrome coronavirus 2 (SARS-CoV2) (Ke et al., 2020; Turoňová et al., 2020; Yao et al., 2020).

In recent years, cryo-ET has also been used to study alpha- and flaviviruses, expanding the horizon on the type of questions that can be asked about these virus structures and life cycles. As cryo-ET does not depend on averages to generate a 3D reconstruction, heterogeneous samples can be imaged, both *in vitro* and *in situ*. Though the resolution achieved with cryo-ET is limited to roughly 20 Å (Frank and McEwen, 1992; Subramaniam et al., 2007), development in sub-tomogram averaging (STA) methods has helped to achieve near-nanometer and sub-nanometer structures of similar sub-volumes extracted from cryo-electron tomograms (Bharat and Scheres, 2016). Cryo-ET with STA has helped to visualize structural intermediates during membrane fusion in CHIKV (Mangala Prasad et al., 2022) as well as study viral assembly intermediates in CHIKV-infected human cells (Chmielewski et al., 2022). Cryo-ET has also been used to delineate pleomorphic maturation intermediates (Plevka et al., 2014) and analyze capsid organization (Tan et al., 2020) in DENV particles. Thus, advancement in cryo-EM methods has immensely contributed to our understanding of these two virus genera which assists us in not only comprehending virus biology but also devising more potent ways to thwart viral infections.

CRediT authorship contribution statement

Kiran Lata: Formal analysis, Data curation, Writing – original draft. **Sylvia Charles:** Data curation. **Vidya Mangala Prasad:** Writing – review & editing, Supervision, Resources, Funding acquisition.

Declaration of Competing Interest

The authors declare that they have no known competing financial interests or personal relationships that could have appeared to influence the work reported in this paper.

Data availability

This is a review article

Acknowledgements

We acknowledge Indian Institute of Science, Bangalore for their start-up grant support to V.M.P and IoE postdoctoral fellowship to K.L.

References

Abad-Zapatero, C., Abdel-Meguid, S.S., Johnson, J.E., Leslie, A.G., Rayment, I., Rossmann, M.G., Suck, D., Tsukihara, T., 1980. Structure of southern bean mosaic virus at 2.8 Å resolution. Nature 286, 33–39.

Adams, C., Carbaugh, D.L., Shu, B., Ng, T.S., Castillo, I.N., Bhowmik, R., Segovia-Chumbez, B., Puhl, A.C., Graham, S., Diehl, S.A., Lazear, H.M., Lok, S.M., de Silva, A. M., Premkumar, L., 2023. Structure and neutralization mechanism of a human antibody targeting a complex Epitope on Zika virus. PLoS Pathog. 19 (1), e1010814.
Adouchief, S., Smura, T., Sane, J., Vapalahti, O., Kurkela, S., 2016. Sindbis virus as a human pathogen-epidemiology, clinical picture and pathogenesis. Rev. Med. Virol. 26, 221–241.
Adrian, M., Dubochet, J., Lepault, J., McDowall, A.W., 1984. Cryo-electron microscopy of viruses. Nature 308, 32–36.
Afonine, P.V., Poon, B.K., Read, R.J., Sobolev, O.V., Terwilliger, T.C., Urzhumtsev, A., Adams, P.D., 2018. Real-space refinement in PHENIX for cryo-EM and crystallography. Acta crystallographica. Section D, Struct. Biol. 74, 531–544.
Allison, S.L., Schalich, J., Stiasny, K., Mandl, C.W., Kunz, C, Heinz, F.X., 1995. Oligomeric rearrangement of tick-borne encephalitis virus envelope proteins induced by an acidic pH. J. Virol. 69 (2), 695–700.
Allison, S.L., Tao, Y.J., O'Riordain, G., Mandl, C.W., Harrison, S.C., Heinz, F.X., 2003. Two distinct size classes of immature and mature subviral particles from tick-borne encephalitis virus. J. Virol. 77, 11357–11366.
Aréchiga-Ceballos, N., Aguilar-Setién, A.J.R.S.T., 2015. Alphaviral equine encephalomyelitis (Eastern, Western and Venezuelan). Rev. Sci. Tech. 34, 491–501.
Baker, M.L., Ju, T., Chiu, W., 2007. Identification of secondary structure elements in intermediate-resolution density maps. Structure 15, 7–19.
Bammes, B.E., Rochat, R.H., Jakana, J., Chiu, W., 2011. Practical performance evaluation of a 10k× 10k CCD for electron cryo-microscopy. J. Struct. Biol. 175, 384–393.
Barton, B., Rhinow, D., Walter, A., Schröder, R., Benner, G., Majorovits, E., Matijevic, M., Niebel, H., Müller, H., Haider, M.J.U., 2011. In-focus electron microscopy of frozen-hydrated biological samples with a Boersch phase plate. Ultramicroscopy 111, 1696–1705.
Basore, K., Kim, A.S., Nelson, C.A., Zhang, R., Smith, B.K., Uranga, C., Vang, L., Cheng, M., Gross, M.L., Smith, J., Diamond, M.S., Fremont, D.H., 2019. Cryo-EM Structure of Chikungunya Virus in Complex with the Mxra8 Receptor. Cell 177, 1725–1737.e1716.
Basore, K., Ma, H., Kafai, N.M., Mackin, S., Kim, A.S., Nelson, C.A., Diamond, M.S., Fremont, D.H., 2021. Structure of Venezuelan equine encephalitis virus in complex with the LDLRAD3 receptor. Nature 598, 672–676.
Battisti, A.J., Yoder, J.D., Plevka, P., Winkler, D.C., Mangala Prasad, V., Kuhn, R.J., Frey, T.K., Steven, A.C., Rossmann, M.G., 2012. Cryo-electron tomography of rubella virus. J. Virol. 86, 11078–11085.
Bharat, T.A., Scheres, S.H.J.N.P., 2016. Resolving macromolecular structures from electron cryo-tomography data using subtomogram averaging in RELION. Nature Protocols 11, 2054–2065.
Bharat, T.A., Noda, T., Riches, J.D., Kraehling, V., Kolesnikova, L., Becker, S., Kawaoka, Y., Briggs, J.A., 2012. Structural dissection of Ebola virus and its assembly determinants using cryo-electron tomography. Proc. Nat. Acad. Sci. 109, 4275–4280.
Bogovic, P, Strle, F, 2015. Tick-borne encephalitis: A review of epidemiology, clinical characteristics, and management. World J. Clin. Cases 3 (5), 430–441.
Brasil, P., Pereira Jr, J.P., Moreira, M.E., Ribeiro Nogueira, R.M., Damasceno, L., Wakimoto, M., Rabello, R.S., Valderramos, S.G., Halai, U.-A., Salles, T.S., 2016. Zika virus infection in pregnant women in Rio de Janeiro. N. Engl. J. Med. 375, 2321–2334.
Button, J.M., Qazi, S.A., Wang, J.C., Mukhopadhyay, S., 2020. Revisiting an old friend: new findings in alphavirus structure and assembly. Curr Opin Virol 45, 25–33.
Byk, L.A., Gamarnik, A.V., 2016. Properties and Functions of the Dengue Virus Capsid Protein. Annu. Rev. Virol. 3 (1), 263–281. https://doi.org/10.1146/annurev-virology-110615-042334.
Cao-Lormeau, V.-M., Blake, A., Mons, S., Lastère, S., Roche, C., Vanhomwegen, J., Dub, T., Baudouin, L., Teissier, A., Larre, P., 2016. Guillain-Barré Syndrome outbreak associated with Zika virus infection in French Polynesia: a case-control study. Lancet 387, 1531–1539.
Carod-Artal, F.J., Wichmann, O., Farrar, J., Gascon, J., 2013. Neurological complications of dengue virus infection. Lancet Neurol. 12, 906–919.
Carragher, B., Kisseberth, N., Kriegman, D., Milligan, R.A., Potter, C.S., Pulokas, J., Reilein, A., 2000. Leginon: an automated system for acquisition of images from vitreous ice specimens. J. Struct. Biol. 132, 33–45.
Chao, L.H., Klein, D.E., Schmidt, A.G., Peña, J.M., Harrison, S.C., 2014. Sequential conformational rearrangements in flavivirus membrane fusion. Elife 3, e04389.
Chen, V.B., Arendall, W.B., Headd, J.J., Keedy, D.A., Immormino, R.M., Kapral, G.J., Murray, L.W., Richardson, J.S., Richardson, D.C., 2010. MolProbity: all-atom structure validation for macromolecular crystallography. Acta Crystallogr. D Biol. Crystallogr. 66, 12–21.
Chen, CL, Klose, T, Sun, C, Kim, AS, Buda, G, Rossmann, MG, Diamond, MS, Klimstra, WB, Kuhn, RJ, 2022. Cryo-EM structures of alphavirus conformational intermediates in low pH-triggered prefusion states. Proc. Natl. Acad. Sci. U. S. A. 119 (30).
Chen, C.L., Hasan, S.S., Klose, T., Sun, Y., Buda, G., Sun, C., Klimstra, W.B., Rossmann, M. G., 2020. Cryo-EM structure of eastern equine encephalitis virus in complex with heparan sulfate analogues. Proc. Nat. Acad. Sci. 117, 8890–8899.
Chen, L., Wang, M., Zhu, D., Sun, Z., Ma, J., Wang, J., Kong, L., Wang, S., Liu, Z., Wei, L., He, Y., Wang, J., Zhang, X., 2018. Implication for alphavirus host-cell entry and assembly indicated by a 3.5A resolution cryo-EM structure. Nat. Commun. 9, 5326.
Chiu, W., Downing, K., Dubochet, J., 1986. Cryoprotection in electron microscopy. J. Microsc. (Oxford) 141, 385–391.
Chiu, W., Schmid, M.F., 1997. Pushing back the limits of electron cryomicroscopy. Nat. Struct. Biol. 4, 331–333.
Chmielewski, D., Schmid, M.F., Simmons, G., Jin, J., Chiu, W., 2022. Chikungunya virus assembly and budding visualized in situ using cryogenic electron tomography. Nat. Microbiol. 7, 1270–1279.
Choi, H.-K., Tong, L., Minor, W., Dumas, P., Boege, U., Rossmann, M.G., Wengler, G., 1991. Structure of Sindbis virus core protein reveals a chymotrypsin-like serine proteinase and the organization of the virion. Nature 354, 37–43.
Chung, S.-C., Lin, H.-H., Niu, P.-Y., Huang, S.-H., Tu, I., Chang, W.-H., 2020. Pre-pro is a fast pre-processor for single-particle cryo-EM by enhancing 2D classification. Commun. Biol. 3, 1–12.
Cowtan, K., 2006. The Buccaneer software for automated model building. 1. Tracing protein chains. Acta crystallographica. Section D, Biological crystallography 62, 1002–1011.
Crowther, R., Amos, L.A., Finch, J., De Rosier, D., Klug, A., 1970a. Three dimensional reconstructions of spherical viruses by Fourier synthesis from electron micrographs. Nature 226, 421–425.
Crowther, R.A., Amos, L.A., 1972. Three-dimensional image reconstructions of some small spherical viruses. In: Cold Spring Harbor symposia on quantitative biology, Vol. 36. Cold Spring Harbor Laboratory Press, pp. 489–494.
Crowther, R.A., DeRosier, D., Klug, A., 1970b. The reconstruction of a three-dimensional structure from projections and its application to electron microscopy. Proc. Roy. Soc. London. A. Math. Phys. Sci. 317, 319–340.
Centers for Disease Control and Prevention (CDC). 1995. Arboviral disease–United States, 1994. MMWR Morb Mortal Wkly Rep., 44(35), 641–644.
Crowther, R.A., Kiselev, N.A., Böttcher, B., Berriman, J.A., Borisova, G.P., Ose, V., Pumpens, P., 1994. Three-dimensional structure of hepatitis B virus core particles determined by electron cryomicroscopy. Cell 77, 943–950.
de la Rosa-Trevín, J.M., Quintana, A., del Cano, L., Zaldívar, A., Foche, I., Gutiérrez, J., Gómez-Blanco, J., Burguet-Castell, J., Cuenca-Alba, J., Abrishami, V., Vargas, J., Otón, J., Sharov, G., Vilas, J.L., Navas, J., Conesa, P., Kazemi, M., Marabini, R., Sorzano, C.O.S., Carazo, J.M., 2016. Scipion: A software framework toward integration, reproducibility and validation in 3D electron microscopy. J. Struct. Biol. 195, 93–99.
De Rosier, D., Klug, A., 1968. Reconstruction of three dimensional structures from electron micrographs. Nature 217, 130–134.
Deresiewicz, R.L., Thaler, S.J., Hsu, L., Zamani, A.A., 1997. Clinical and neuroradiographic manifestations of eastern equine encephalitis. N. Engl. J. Med. 336, 1867–1874.
DiNunno, N.M., Goetschius, D.J., Narayanan, A., Majowicz, S.A., Moustafa, I., Bator, C. M., Hafenstein, S.L., Jose, J., 2020. Identification of a pocket factor that is critical to Zika virus assembly. Nat. Commun. 11, 4953.
A Dowd K, Sirohi D, D Speer S, VanBlargan LA, Chen RE, Mukherjee S, Whitener BM, Govero J, Aleshnick M, Larman B, Sukupolvi-Petty S, Sevvana M, Miller AS, Klose T, Zheng A, Koenig S, Kielian M, Kuhn RJ, Diamond MS, Pierson TC. prM-reactive antibodies reveal a role for partially mature virions in dengue virus pathogenesis. Proc Natl Acad Sci U S A. 2023 Jan 17;120(3).
Dubochet, J., Chang, J.-J., Freeman, R., Lepault, J., McDowall, A., 1982a. Frozen aqueous suspensions. Ultramicroscopy 10, 55–61.
Dubochet, J., Lepault, J., Freeman, R., Berriman, J., Homo, J.C., 1982b. Electron microscopy of frozen water and aqueous solutions. J. Microsc. 128, 219–237.
Elmlund, D., Elmlund, H., 2012. SIMPLE: Software for ab initio reconstruction of heterogeneous single-particles. J. Struct. Biol. 180, 420–427.
Elmlund, H., Elmlund, D., Bengio, S., 2013. PRIME: Probabilistic Initial 3D Model Generation for Single-Particle Cryo-Electron Microscopy. Structure 21, 1299–1306.
Emsley, P., Cowtan, K., 2004. Coot: model-building tools for molecular graphics. Acta Crystallogr. D Biol. Crystallogr. 60, 2126–2132.
Fang, Q., Zhu, D., Agarkova, I., Adhikari, J., Klose, T., Liu, Y., Chen, Z., Sun, Y., Gross, M. L., Van Etten, J.L., Zhang, X., Rossmann, M.G., 2019. Near-atomic structure of a giant virus. Nat. Commun. 10, 388.
Farmer, J., Suhrbier, A., 2019. Interpreting paired serology for Ross River virus and Barmah Forest virus diseases. Australian Journal for General Practitioners 48, 645–649.
Ferlenghi, I., Clarke, M., Ruttan, T., Allison, S.L., Schalich, J., Heinz, F.X., Harrison, S.C., Rey, F.A., Fuller, S.D., 2001. Molecular organization of a recombinant subviral particle from tick-borne encephalitis virus. Mol. Cell 7, 593–602.
Fibriansah, G., Tan, J.L., Smith, S.A., de Alwis, A.R., Ng, T.S., Kostyuchenko, V.A., Ibarra, K.D., Wang, J., Harris, E., de Silva, A., Crowe Jr., J.E., Lok, S.M., 2014. A potent anti-dengue human antibody preferentially recognizes the conformation of E protein monomers assembled on the virus surface. EMBO Mol. Med. 6 (3), 358–371.
Fibriansah, G., Ng, T.S., Kostyuchenko, V.A., Lee, J., Lee, S., Wang, J., Lok, S.M., 2013. Structural changes in dengue virus when exposed to a temperature of 37°C. J Virol 87, 7585–7592.
Fibriansah, G., Ibarra, K.D., Ng, T.-S., Smith, S.A., Tan, J.L., Lim, X.-N., Ooi, J.S.G., Kostyuchenko, V.A., Wang, J., de Silva, A.M., Harris, E., Crowe, J.E., Lok, S.-M., 2015. Cryo-EM structure of an antibody that neutralizes dengue virus type 2 by locking. E protein dimers 349, 88–91.
Frank, J., 1990. Classification of macromolecular assemblies studied as 'single particles'. Q. Rev. Biophys. 23, 281–329.
Frank, J., McEwen, B.F., 1992. Alignment by cross-correlation. In: *Electron tomography: three-dimensional imaging with the transmission electron microscope*. Springer US, Boston, MA, pp. 205–213.
Frank, J., Radermacher, M., Penczek, P., Zhu, J., Li, Y., Ladjadj, M., Leith, A., 1996. SPIDER and WEB: processing and visualization of images in 3D electron microscopy and related fields. J. Struct. Biol. 116, 190–199.
Fu, S., Song, S., Liu, H., Li, Y., Li, X., Gao, X., Xu, Z., Liu, G., Wang, D., Tian, Z., Zhou, J., He, Y., Lei, W., Wang, H., Wang, B., Lu, X., Liang, G., 2017. ZIKA virus isolated from

mosquitoes: a field and laboratory investigation in China, 2016. Sci. China Life Sci. 60, 1364–1371.
Fuller, S.D., 1987. The T= 4 envelope of Sindbis virus is organized by interactions with a complementary T= 3 capsid. Cell 48, 923–934.
Fuller, S.D., Berriman, J.A., Butcher, S.J., Gowen, B.E., 1995. Low pH induces swiveling of the glycoprotein heterodimers in the Semliki Forest virus spike complex. Cell 81, 715–725.
Fuzik, T., Formanova, P., Ruzek, D., Yoshii, K., Niedrig, M., Plevka, P., 2018. Structure of tick-borne encephalitis virus and its neutralization by a monoclonal antibody. Nat. Commun. 9, 436.
Goddard, T.D., Huang, C.C., Meng, E.C., Pettersen, E.F., Couch, G.S., Morris, J.H., Ferrin, T.E., 2018. UCSF ChimeraX: Meeting modern challenges in visualization and analysis. Protein Sci. 27, 14–25.
Goetschius, D.J., Lee, H., Hafenstein, S., 2019. CryoEM reconstruction approaches to resolve asymmetric features. Adv. Virus Res. 105, 73–91.
Grant, T., Rohou, A., Grigorieff, N., 2018. cisTEM, user-friendly software for single-particle image processing. Elife 7, e35383.
Griffin, D., 2013. Chapter 23: Alphaviruses, p 652-770. Knipe DM, Howley PM 689.
Griffiths, M.J., Turtle, L., Solomon, T., 2014. Chapter 26 - Japanese encephalitis virus infection. In: Tselis, A.C., Booss, J. (Eds.), Handbook of Clinical Neurology. Elsevier, pp. 561–576.
Grigorieff, N., 2007. FREALIGN: high-resolution refinement of single particle structures. J. Struct. Biol. 157, 117–125.
Grigorieff, N., 2016. Frealign: An Exploratory Tool for Single-Particle Cryo-EM. Methods Enzymol. 579, 191–226.
Guo, F., Jiang, W., 2014. Single particle cryo-electron microscopy and 3-D reconstruction of viruses. Methods Mol Biol 1117, 401–443.
Halldorsson, S., Li, S., Li, M., Harlos, K., Bowden, T.A., Huiskonen, J.T., 2018. Shielding and activation of a viral membrane fusion protein. Nat. Commun. 9.
Halstead, S.B., 2007. Dengue. The lancet 370, 1644–1652.
Harauz, G., van Heel, M., 1986. Exact filters for general geometry three dimensional reconstruction. Optik 73, 146–156.
Hardy, J.M., Newton, N.D., Modhiran, N., Scott, C.A.P., Venugopal, H., Vet, L.J., Young, P.R., Hall, R.A., Hobson-Peters, J., Coulibaly, F., Watterson, D., 2021. A unified route for flavivirus structures uncovers essential pocket factors conserved across pathogenic viruses. Nat. Commun. 12, 3266.
Harris, A., Cardone, G., Winkler, D.C., Heymann, J.B., Brecher, M., White, J.M., Steven, A.C., 2006. Influenza virus pleiomorphy characterized by cryoelectron tomography. Proc. Natl. Acad. Sci. U. S. A. 103 (50), 19123–19127.
Harrison, S., Olson, A., Schutt, C., Winkler, F., Bricogne, G., 1978. Tomato bushy stunt virus at 2.9 Å resolution. Nature 276, 368–373.
Hasan, S.S., Sevvana, M., Kuhn, R.J., Rossmann, M.G., 2018a. Structural biology of Zika virus and other flaviviruses. Nat. Struct. Mol. Biol. 25, 13–20.
Hasan, S.S., Sun, C., Kim, A.S., Watanabe, Y., Chen, C.-L., Klose, T., Buda, G., Crispin, M., Diamond, M.S., Klimstra, W.B., 2018b. Cryo-EM structures of eastern equine encephalitis virus reveal mechanisms of virus disassembly and antibody neutralization. Cell Rep. 25 (3136–3147), e3135.
Hasan, S.S., Sun, C., Kim, A.S., Watanabe, Y., Chen, C.L., Klose, T., Buda, G., Crispin, M., Diamond, M.S., Klimstra, W.B., Rossmann, M.G., 2018c. Cryo-EM Structures of Eastern Equine Encephalitis Virus Reveal Mechanisms of Virus Disassembly and Antibody Neutralization. Cell Rep 25 (3136–3147), e3135.
Henderson, R., Glaeser, R.M., 1985. Quantitative analysis of image contrast in electron micrographs of beam-sensitive crystals. Ultramicroscopy 16, 139–150.
Henderson, R., Chen, S., Chen, J.Z., Grigorieff, N., Passmore, L.A., Ciccarelli, L., Rubinstein, J.L., Crowther, R.A., Stewart, P.L., Rosenthal, P.B., 2011. Tilt-pair analysis of images from a range of different specimens in single-particle electron cryomicroscopy. J. Mol. Biol. 413, 1028–1046.
Hernandez, R., Brown, D.T., Paredes, A., 2014. Structural differences observed in arboviruses of the alphavirus and flavivirus genera. Adv Virol 2014, 259382.
Hogle, J., Chow, M., Filman, D., 1985. Three-dimensional structure of poliovirus at 2.9 Å resolution. Science 229, 1358–1365.
Hohn, M., Tang, G., Goodyear, G., Baldwin, P.R., Huang, Z., Penczek, P.A., Yang, C., Glaeser, R.M., Adams, P.D., Ludtke, S.J., 2007. SPARX, a new environment for Cryo-EM image processing. J. Struct. Biol. 157, 47–55.
Holmes, A.C., Basore, K., Fremont, D.H., Diamond, M.S., 2020. A molecular understanding of alphavirus entry. PLoS Pathog. 16, e1008876.
Honein, M.A., Dawson, A.L., Petersen, E.E., Jones, A.M., Lee, E.H., Yazdy, M.M., Ahmad, N., Macdonald, J., Evert, N., Bingham, A., 2017. Birth defects among fetuses and infants of US women with evidence of possible Zika virus infection during pregnancy. JAMA 317, 59–68.
Huang, Q.J., Song, K., Xu, C., Bolon, D.N.A., Wang, J.P., Finberg, R.W., Schiffer, C.A., Somasundaran, M., 2022. Quantitative structural analysis of influenza virus by cryo-electron tomography and convolutional neural networks. Structure 30, 777–786. e773.
Ilca, S.L., Kotecha, A., Sun, X., Poranen, M.M., Stuart, D.I., Huiskonen, J.T., 2015. Localized reconstruction of subunits from electron cryomicroscopy images of macromolecular complexes. Nat. Commun. 6, 8843.
Jose, J., Snyder, J.E., Kuhn, R.J., 2009. A structural and functional perspective of alphavirus replication and assembly. Future Microbiol. 4, 837–856.
Kafai, N.M., Williamson, L.E., Binshtein, E., Sukupolvi-Petty, S., Gardner, C.L., Liu, J., Mackin, S., Kim, A.S., Kose, N., Carnahan, R.H., Jung, A., Droit, L., Reed, D.S., Handley, S.A., Klimstra, W.B., Crowe, J.E., Diamond, M.S., 2022. Neutralizing antibodies protect mice against Venezuelan equine encephalitis virus aerosol challenge. J. Exp. Med. 219.
Ke, Z., Oton, J., Qu, K., et al., 2020. Structures and distributions of SARS-CoV-2 spike proteins on intact virions. Nature 588, 498–502. https://doi.org/10.1038/s41586-020-2665-2.
Khare, B., Klose, T., Fang, Q., Rossmann, M.G., Kuhn, R.J., 2021. Structure of Usutu virus SAAR-1776 displays fusion loop asymmetry. Proc. Natl. Acad. Sci. U. S. A. 118 (34).
Kivioja, T., Ravantti, J., Verkhovsky, A., Ukkonen, E., Bamford, D., 2000. Local average intensity-based method for identifying spherical particles in electron micrographs. J. Struct. Biol. 131, 126–134.
Klose, T., Reteno, D.G., Benamar, S., Hollerbach, A., Colson, P., La Scola, B., Rossmann, M.G., 2016. Structure of faustovirus, a large dsDNA virus. Proc. Nat. Acad. Sci. 113, 6206–6211.
Kostyuchenko, V.A., Jakana, J., Liu, X., Haddow, A.D., Aung, M., Weaver, S.C., Chiu, W., Lok, S.-M., 2011. The structure of barmah forest virus as revealed by cryo-electron microscopy at a 6-angstrom resolution has detailed transmembrane protein architecture and interactions. J. Virol. 85, 9327–9333.
Kostyuchenko, V.A., Zhang, Q., Tan, J.L., Ng, T.S., Lok, S.M., 2013. Immature and mature dengue serotype 1 virus structures provide insight into the maturation process. J. Virol. 87, 7700–7707.
Kostyuchenko, V.A., Chew, P.L., Ng, T.-S., Lok, S.-M., 2014. Near-atomic resolution cryo-electron microscopic structure of dengue serotype 4 virus. J. Virol. 88, 477–482.
Kostyuchenko, V.A., Lim, E.X., Zhang, S., Fibriansah, G., Ng, T.S., Ooi, J.S., Shi, J., Lok, S.M., 2016. Structure of the thermally stable Zika virus. Nature 533, 425–428.
Kuhn, R., 2007. Togaviridae: the viruses and their replication. Fields virology 1, 1001–1022.
Kuhn, R.J., 2013. Chapter 22: Togaviradae, p 629–650. In: *Virology*. Lippincott Williams & Wilkins, Philadelphia.
Kuhn, R.J., Zhang, W., Rossmann, M.G., Pletnev, S.V., Corver, J., Lenches, E., Jones, C.T., Mukhopadhyay, S., Chipman, P.R., Strauss, E.G., 2002. Structure of dengue virus: implications for flavivirus organization, maturation, and fusion. Cell 108, 717–725.
Lander, G.C., Stagg, S.M., Voss, N.R., Cheng, A., Fellmann, D., Pulokas, J., Yoshioka, C., Irving, C., Mulder, A., Lau, P.-W., 2009. Appion: an integrated, database-driven pipeline to facilitate EM image processing. J. Struct. Biol. 166, 95–102.
Laskowski, R.A., MacArthur, M.W., Moss, D.S., Thornton, J.M., 1993. PROCHECK: a program to check the stereochemical quality of protein structures. J. Appl. Cryst. 26, 283–291.
Lee, S., Owen, K.E., Choi, H.K., Lee, H., Lu, G., Wengler, G., Brown, D.T., Rossmann, M. G., Kuhn, R.J., 1996. Identification of a protein binding site on the surface of the alphavirus nucleocapsid and its implication in virus assembly. Structure 4, 531–541.
Lescar, J., Roussel, A., Wien, M.W., Navaza, J., Fuller, S.D., Wengler, G., Wengler, G., Rey, F.A., 2001. The Fusion glycoprotein shell of Semliki Forest virus: an icosahedral assembly primed for fusogenic activation at endosomal pH. Cell 105, 137–148.
Li, X., Mooney, P., Zheng, S., Booth, C.R., Braunfeld, M.B., Gubbens, S., Agard, D.A., Cheng, Y., 2013. Electron counting and beam-induced motion correction enable near-atomic-resolution single-particle cryo-EM. Nat. Methods 10, 584–590.
Li, X., Zheng, S., Agard, D.A., Cheng, Y., 2015. Asynchronous data acquisition and on-the-fly analysis of dose fractionated cryoEM images by UCSFImage. J. Struct. Biol. 192, 174–178.
Liljas, L., Unge, T., Jones, T.A., Fridborg, K., Lövgren, S., Skoglund, U., Strandberg, B., 1982. Structure of satellite tobacco necrosis virus at 3.0 Å resolution. J. Mol. Biol. 159, 93–108.
Lim, X.X., Shu, B., Zhang, S., Tan, A.W.K., Ng, T.S., Lim, X.N., Chew, V.S., Shi, J., Screaton, G.R., Lok, S.M., Anand, G.S., 2021. Human antibody C10 neutralizes by diminishing Zika but enhancing dengue virus dynamics. Cell 184, 6067–6080.e6013.
Liu, X., Jiang, W., Jakana, J., Chiu, W., 2007. Averaging tens to hundreds of icosahedral particle images to resolve protein secondary structure elements using a Multi-Path Simulated Annealing optimization algorithm. J. Struct. Biol. 160, 11–27.
Liu, H., Zhang, X., Li, L.-X., Shi, N., Sun, X.-T., Liu, Q., Jin, N.-Y., Si, X.-K., 2019. First isolation and characterization of Getah virus from cattle in northeastern China. BMC Vet. Res. 15, 1–7.
Long, F., Doyle, M., Fernandez, E., Miller, A.S., Klose, T., Sevvana, M., Bryan, A., Davidson, E., Doranz, B.J., Kuhn, R.J., Diamond, M.S., Crowe Jr., J.E., Rossmann, M. G., 2019. Structural basis of a potent human monoclonal antibody against Zika virus targeting a quaternary epitope. Proc Natl Acad Sci U S A 116, 1591–1596.
Louten, J., 2016. Virus structure and classification. Essential human virology 19.
Ludtke, S.J., Baldwin, P.R., Chiu, W., 1999. EMAN: semiautomated software for high-resolution single-particle reconstructions. J. Struct. Biol. 128, 82–97.
Ma, B., Huang, C., Ma, J., Xiang, Y., Zhang, X., 2021. Structure of Venezuelan equine encephalitis virus with its receptor LDLRAD3. Nature 598, 677–681.
Mancini, E.J., Clarke, M., Gowen, B.E., Rutten, T., Fuller, S.D., 2000. Cryo-electron microscopy reveals the functional organization of an enveloped virus, Semliki Forest virus. Mol. Cell 5, 255–266.
Mangala Prasad, V., Klose, T., Rossmann, M.G., 2017. Assembly, maturation and three-dimensional helical structure of the teratogenic rubella virus. PLoS Pathog. 13, e1006377.
Mangala Prasad, V., Blijleven, J.S., Smit, J.M., Lee, K.K., 2022. Visualization of conformational changes and membrane remodeling leading to genome delivery by viral class-II fusion machinery. Nat. Commun. 13, 4772.
Mangala Prasad, V., Leaman, D.P., Lovendahl, K.N., Croft, J.T., Benhaim, M.A., Hodge, E. A., Zwick, M.B., Lee, K.K., 2022. Cryo-ET of Env on intact HIV virions reveals structural variation and positioning on the Gag lattice. Cell 185 (4), 641–653.
Mastronarde, D.N., 2005. Automated electron microscope tomography using robust prediction of specimen movements. J. Struct. Biol. 152, 36–51.
Mattei, S., Glass, B., Hagen, W.J., Kräusslich, H.G., Briggs, J.A., 2016. The structure and flexibility of conical HIV-1 capsids determined within intact virions. Science. 354 (6318), 1434–1437.

McMullan, G., Chen, S., Henderson, R., Faruqi, A., 2009. Detective quantum efficiency of electron area detectors in electron microscopy. Ultramicroscopy 109, 1126–1143.
Mindell, J.A., Grigorieff, N., 2003. Accurate determination of local defocus and specimen tilt in electron microscopy. J. Struct. Biol. 142 (3), 334–347.
Morrone, S.R., Chew, V.S.Y., Lim, X.-N., Ng, T.-S., Kostyuchenko, V.A., Zhang, S., Wirawan, M., Chew, P.-L., Lee, J., Tan, J.L., Wang, J., Tan, T.Y., Shi, J., Screaton, G., Morais, M.C., Lok, S.-M., 2020. High flavivirus structural plasticity demonstrated by a non-spherical morphological variant. Nat. Commun. 11, 3112.
Mourya, D.T., Thakare, J.R., Gokhale, M.D., Powers, A.M., Hundekar, S.L., Jayakumar, P. C., Bondre, V.P., Shouche, Y.S., Padbidri, V.S., 2001. Isolation of chikungunya virus from Aedes aegypti mosquitoes collected in the town of Yawat, Pune District, Maharashtra State, India. Acta Virol. 45, 305–309.
Mukherjee, S., Sirohi, D., Dowd, K.A., Chen, Z., Diamond, M.S., Kuhn, R.J., Pierson, T.C., 2016. Enhancing dengue virus maturation using a stable furin over-expressing cell line. Virology 497, 33–40.
Mukhopadhyay, S., Chipman, P.R., Hong, E.M., Kuhn, R.J., Rossmann, M.G., 2002. In vitro-assembled alphavirus core-like particles maintain a structure similar to that of nucleocapsid cores in mature virus. J. Virol. 76, 11128–11132.
Mukhopadhyay, S., Kim, B.S., Chipman, P.R., Rossmann, M.G., Kuhn, R.J., 2003. Structure of West Nile virus. Science 302, 248.
Mukhopadhyay, S., Kuhn, R.J., Rossmann, M.G., 2005. A structural perspective of the flavivirus life cycle. Nat Rev Microbiol 3, 13–22.
Mukhopadhyay, S., Zhang, W., Gabler, S., Chipman, P.R., Strauss, E.G., Strauss, J.H., Baker, T.S., Kuhn, R.J., Rossmann, M.G., 2006. Mapping the structure and function of the E1 and E2 glycoproteins in alphaviruses. Structure 14, 63–73.
Namba, K., Stubbs, G., 1986. Structure of Tobacco Mosaic Virus at 3.6 & #xc5; Resolution: Implications for Assembly. Science 231, 1401–1406.
Nelson, S., Hernandez, R., Ferreira, D., Brown, D.T., 2005. In vivo processing and isolation of furin protease-sensitive alphavirus glycoproteins: a new technique for producing mutations in virus assembly. Virology 332, 629–639.
Newton, N.D., Hardy, J.M., Modhiran, N., Hugo, L.E., Amarilla, A.A., Bibby, S., Venugopal, H., Harrison, J.J., Traves, R.J., Hall, R.A., 2021. The structure of an infectious immature flavivirus redefines viral architecture and maturation. Sci. Adv. 7, eabe4507.
Noda, T., 2011. Native morphology of influenza virions. Front. Microbiol. 2, 269.
Nogales, E., Scheres, S.H., 2015. Cryo-EM: A Unique Tool for the Visualization of Macromolecular Complexity. Mol. Cell 58, 677–689.
Owen, K.E., Kuhn, R.J., 1997. Alphavirus Budding Is Dependent on the Interaction between the Nucleocapsid and Hydrophobic Amino Acids on the Cytoplasmic Domain of the E2 Envelope Glycoprotein. Virology 230, 187–196.
Paredes, A.M., Brown, D.T., Rothnagel, R., et al., 1993. Three-dimensional structure of a membrane-containing virus. Proc. Natl. Acad. Sci. U. S. A. 90 (19), 9095–9099.
Passi, D., Sharma, S., Dutta, S.R., Ahmed, M., 2017. Zika virus diseases–the new face of an ancient enemy as global public health emergency (2016): brief review and recent updates. International Journal of. Prev. Med. 8.
Pereira, J., Lamzin, V.S., 2017. A distance geometry-based description and validation of protein main-chain conformation. IUCrJ 4, 657–670.
Petersen, L.R., Brault, A.C., Nasci, R.S., 2013. West Nile virus: review of the literature. JAMA 310, 308–315.
Pettersen, E.F., Goddard, T.D., Huang, C.C., Couch, G.S., Greenblatt, D.M., Meng, E.C., Ferrin, T.E., 2004. UCSF Chimera—a visualization system for exploratory research and analysis. J. Comput. Chem. 25, 1605–1612.
Peukes, J., Xiong, X., Erlendsson, S., Qu, K., Wan, W., Calder, L.J., Schraidt, O., Kummer, S., Freund, S.M.V., Kräusslich, H.G., Briggs, J.A.G., 2020. The native structure of the assembled matrix protein 1 of influenza A virus. Nature 587, 495–498.
Pletnev, S.V., Zhang, W., Mukhopadhyay, S., Fisher, B.R., Hernandez, R., Brown, D.T., Baker, T.S., Rossmann, M.G., Kuhn, R.J., 2001. Locations of carbohydrate sites on alphavirus glycoproteins show that E1 forms an icosahedral scaffold. Cell 105, 127–136.
Plevka, P., Perera, R., Cardosa, J., Kuhn, R.J., Rossmann, M.G., 2012. Crystal structure of human enterovirus 71. Science 336, 1274.
Plevka, P., Battisti, A.J., Sheng, J., Rossmann, M.G., 2014. Mechanism for maturation-related reorganization of flavivirus glycoproteins. J. Struct. Biol. 185, 27–31.
Plourde, A.R., Bloch, E.M., 2016. A Literature Review of Zika Virus. Emerg. Infect. Dis. 22, 1185–1192.
Pokidysheva, E., Zhang, Y., Battisti, A.J., Bator-Kelly, C.M., Chipman, P.R., Xiao, C., Gregorio, G.G., Hendrickson, W.A., Kuhn, R.J., Rossmann, M.G., 2006. Cryo-EM reconstruction of dengue virus in complex with the carbohydrate recognition domain of DC-SIGN. Cell 124, 485–493.
Powell, L.A., Miller, A., Fox, J.M., Kose, N., Klose, T., Kim, A.S., Bombardi, R., Tennekoon, R.N., Dharshan de Silva, A., Carnahan, R.H., Diamond, M.S., Rossmann, M.G., Kuhn, R.J., Crowe Jr., J.E., 2020. Human mAbs Broadly Protect against Arthritogenic Alphaviruses by Recognizing Conserved Elements of the Mxra8 Receptor-Binding Site. Cell Host Microbe 28, 699–711.e697.
Prasad, V.M., Miller, A.S., Klose, T., Sirohi, D., Buda, G., Jiang, W., Kuhn, R.J., Rossmann, M.G., 2017. Structure of the immature Zika virus at 9 A resolution. Nature Structural Molecular Biology 24, 184–186.
Pulkkinen, L.I.A., Barrass, S.V., Domanska, A., Överby, A.K., Anastasina, M., Butcher, S. J., 2022. Molecular Organisation of Tick-Borne Encephalitis Virus. Viruses 14, 792.
Punjani, A., Rubinstein, J.L., Fleet, D.J., Brubaker, M.A., 2017. cryoSPARC: algorithms for rapid unsupervised cryo-EM structure determination. Nat. Methods 14, 290–296.
Qiu, X., Lei, Y., Yang, P., Gao, Q., Wang, N., Cao, L., Yuan, S., Huang, X., Deng, Y., Ma, W., Ding, T., Zhang, F., Wu, X., Hu, J., Liu, S.L., Qin, C., Wang, X., Xu, Z., Rao, Z., 2018. Structural basis for neutralization of Japanese encephalitis virus by two potent therapeutic antibodies. Nat Microbiol 3, 287–294.
Qu, K., Ke, Z., Zila, V., Anders-Össwein, M., Glass, B., Mücksch, F., Müller, R., Schultz, C., Müller, B., Kräusslich, H.G., Briggs, J.A.G., 2021. Maturation of the matrix and viral membrane of HIV-1. Science 373 (6555), 700–704.
Renner, M., Dejnirattisai, W., Carrique, L., Martin, I.S., Karia, D., Ilca, S.L., Ho, S.F., Kotecha, A., Keown, J.R., Mongkolsapaya, J., Screaton, G.R., Grimes, J.M., 2021. Flavivirus maturation leads to the formation of an occupied lipid pocket in the surface glycoproteins. Nat. Commun. 12, 1238.
Rey, F.A., Heinz, F.X., Mandl, C., Kunz, C., Harrison, S.C.J.N., 1995. The envelope glycoprotein from tick-borne encephalitis virus at 2. Å resolution 375, 291–298.
Rezza, G., Chen, R., Weaver, S.C., 2017. O'nyong-nyong fever: a neglected mosquito-borne viral disease. Pathogens and global health 111, 271–275.
Ribeiro-Filho, H.V., Coimbra, L.D., Cassago, A., Rocha, R.P.F., Guerra, J.V.D.S., de Felicio, R., Carnieli, C.M., Leme, L., Padilha, A.C., Paes Leme, A.F., Trivella, D.B.B., Portugal, R.V., Lopes-de-Oliveira, P.S., Marques, R.E., 2021. Cryo-EM structure of the mature and infective Mayaro virus at 4.4 Å resolution reveals features of arthritogenic alphaviruses. Nat. Commun. 12 (1), 3038.
Roseman, A., 2004. FindEM—a fast, efficient program for automatic selection of particles from electron micrographs. J. Struct. Biol. 145, 91–99.
Rosen, L., 1986. The natural history of Japanese encephalitis virus. Annual Rev. Microbiol. 40, 395–414.
Rosenthal, P.B., Henderson, R., 2003. Optimal determination of particle orientation, absolute hand, and contrast loss in single-particle electron cryomicroscopy. J. Mol. Biol. 333, 721–745.
Rosenthal, P.B., 2015. From high symmetry to high resolution in biological electron microscopy: a commentary on Crowther (1971) 'Procedures for three-dimensional reconstruction of spherical viruses by Fourier synthesis from electron micrographs'. Philos Trans R Soc Lond B Biol Sci., 370(1666), 20140345.
Rossmann, M.G., Arnold, E., Erickson, J.W., Frankenberger, E.A., Griffith, J.P., Hecht, H.-J., Johnson, J.E., Kamer, G., Luo, M., Mosser, A.G., Rueckert, R.R., Sherry, B., Vriend, G., 1985. Structure of a human common cold virus and functional relationship to other picornaviruses. Nature 317, 145–153.
Saxton, W., Frank, J., 1976. Motif detection in quantum noise-limited electron micrographs by cross-correlation. Ultramicroscopy 2, 219–227.
Schatz, M., Orlova, E., Dube, P., Stark, H., Zemlin, F., Van Heel, M., 1997. Angular reconstitution in three-dimensional electron microscopy: Practical and technical aspects. Scanning Microsc. 11, 179–193.
Scheres, S.H., 2012. RELION: implementation of a Bayesian approach to cryo-EM structure determination. J. Struct. Biol. 180, 519–530.
Scheres, S.H., Chen, S., 2012. Prevention of overfitting in cryo-EM structure determination. Nat. Methods 9, 853–854.
Scheres, S.H., Valle, M., Carazo, J.M., 2005a. Fast maximum-likelihood refinement of electron microscopy images. Bioinformatics 21 (Suppl 2), ii243–ii244.
Scheres, S.H., Gao, H., Valle, M., Herman, G.T., Eggermont, P.P., Frank, J., Carazo, J.M., 2007. Disentangling conformational states of macromolecules in 3D-EM through likelihood optimization. Nat. Methods 4, 27–29.
Scheres, S.H., Núñez-Ramírez, R., Sorzano, C.O., Carazo, J.M., Marabini, R., 2008. Image processing for electron microscopy single-particle analysis using XMIPP. Nat. Protoc. 3, 977–990.
Scheres, S.H.W., Valle, M., Nuñez, R., Sorzano, C.O.S., Marabini, R., Herman, G.T., Carazo, J.-M., 2005b. Maximum-likelihood Multi-reference Refinement for Electron Microscopy Images. J. Mol. Biol. 348, 139–149.
Schrag, J.D., Prasad, B.V., Rixon, F.J., Chiu, W., 1989. Three-dimensional structure of the HSV1 nucleocapsid. Cell 56, 651–660.
Sevvana, M., Rogers, T.F., Miller, A.S., Long, F., Klose, T., Beutler, N., Lai, Y.C., Parren, M., Walker, L.M., Buda, G., Burton, D.R., Rossmann, M.G., Kuhn, R.J., 2020. Structural Basis of Zika Virus Specific Neutralization in Subsequent Flavivirus Infections. Viruses 12 (12), 1346.
Sevvana, M., Long, F., Miller, A.S., Klose, T., Buda, G., Sun, L., Kuhn, R.J., Rossmann, M. G., 2018. Refinement and Analysis of the Mature Zika Virus Cryo-EM Structure at 3.1 A Resolution. Structure 26, 1169–1177 e1163.
Sharma, A., Zhang, X., Dejnirattisai, W., Dai, X., Gong, D., Wongwiwat, W., Duquerroy, S., Rouvinski, A., Vaney, M.-C., Guardado-Calvo, P., Haouz, A., England, P., Sun, R., Zhou, Z.H., Mongkolsapaya, J., Screaton, G.R., Rey, F.A., 2021. The epitope arrangement on flavivirus particles contributes to Mab C10's extraordinary neutralization breadth across Zika and dengue viruses. Cell 184, 6052–6066.e6018.
Sigworth, F.J., 1998. A maximum-likelihood approach to single-particle image refinement. J. Struct. Biol. 122, 328–339.
Silva, L.A., Dermody, T.S., 2017. Chikungunya virus: epidemiology, replication, disease mechanisms, and prospective intervention strategies. Journal of Clinical Investigations 127, 737–749.
Singh, T., Hwang, K.K., Miller, A.S., Jones, R.L., Lopez, C.A., Dulson, S.J., Giuberti, C., Gladden, M.A., Miller, I., Webster, H.S., Eudailey, J.A., Luo, K., Von Holle, T., Edwards, R.J., Valencia, S., Burgomaster, K.E., Zhang, S., Mangold, J.F., Tu, J.J., Dennis, M., Alam, S.M., Premkumar, L., Dietze, R., Pierson, T.C., Ooi, E.E., Lazear, H. M., Kuhn, R.J., Permar, S.R., Bonsignori, M., 2022. A Zika virus-specific IgM elicited in pregnancy exhibits ultrapotent neutralization. Cell. 185 (25), 4826–4840.
Sirohi, D., Kuhn, R.J., 2017. Zika Virus Structure, Maturation, and Receptors. J. Infect. Dis. 216 (suppl_10), S935–S944.
Sirohi, D., Chen, Z., Sun, L., Klose, T., Pierson, T.C., Rossmann, M.G., Kuhn, R.J., 2016. The 3.8 Å resolution cryo-EM structure of Zika virus. Science 352, 467–470.
Skoging, U., Vihinen, M., Nilsson, L., Liljeström, P., 1996. Aromatic interactions define the binding of the alphavirus spike to its nucleocapsid. Structure 4, 519–529.
Song, H., Zhao, Z., Chai, Y., Jin, X., Li, C., Yuan, F., Liu, S., Gao, Z., Wang, H., Song, J., Vazquez, L., Zhang, Y., Tan, S., Morel, C.M., Yan, J., Shi, Y., Qi, J., Gao, F., Gao, G.F.,

2019. Molecular Basis of Arthritogenic Alphavirus Receptor MXRA8 Binding to Chikungunya Virus Envelope Protein. Cell 177 (1714–1724), e1712.
Stass, R., Ng, W.M., Kim, Y.C., Huiskonen, J.T., 2019. Structures of enveloped virions determined by cryogenic electron microscopy and tomography. Adv. Virus Res. 105, 35–71.
Strauss, J.H., Strauss, E.G., 1994 Sep. The alphaviruses: gene expression, replication, and evolution. Microbiol. Rev. 58 (3), 491–562.
Strauss, E.G., Rice, C.M., Strauss, J.H., 1984. Complete nucleotide sequence of the genomic RNA of Sindbis virus. Virology 133, 92–110.
Subramaniam, S., Bartesaghi, A., Liu, J., Bennett, A.E., Sougrat, R., 2007. Electron tomography of viruses. Curr. Opin. Struct. Biol. 17, 596–602.
Suhrbier, A., Jaffar-Bandjee, M.C., Gasque, P., 2012. Arthritogenic alphaviruses–an overview. Nat. Rev. Rheumatol. 8, 420–429.
Suloway, C., Pulokas, J., Fellmann, D., Cheng, A., Guerra, F., Quispe, J., Stagg, S., Potter, C.S., Carragher, B., 2005. Automated molecular microscopy: the new Leginon system. J. Struct. Biol. 151, 41–60.
Sun, C., Gonzalez, B., Vago, F.S., Jiang, W., 2021. High resolution single particle Cryo-EM refinement using JSPR. Prog. Biophys. Mol. Biol. 160, 37–42.
Sun, S., Xiang, Y., Akahata, W., Holdaway, H., Pal, P., Zhang, X., Diamond, M.S., Nabel, G.J., Rossmann, M.G., 2013. Structural analyses at pseudo atomic resolution of Chikungunya virus and antibodies show mechanisms of neutralization. Elife 2, e00435.
Suthar, M.S., Diamond, M.S., Gale Jr., M., 2013. West Nile virus infection and immunity. Nat. Rev. Microbiol. 11, 115–128.
Tan, T.Y., Fibriansah, G., Kostyuchenko, V.A., Ng, T.-S., Lim, X.-X., Zhang, S., Lim, X.-N., Wang, J., Shi, J., Morais, M.C., 2020. Capsid protein structure in Zika virus reveals the flavivirus assembly process. Nat. Commun. 11, 895.
Tang, G., Peng, L., Baldwin, P.R., Mann, D.S., Jiang, W., Rees, I., Ludtke, S.J., 2007. EMAN2: an extensible image processing suite for electron microscopy. J. Struct. Biol. 157, 38–46.
Taylor, S.F., Patel, P.R., Herold, T.J., 2005. Recurrent arthralgias in a patient with previous Mayaro fever infection. South. Med. J. 98, 484–485.
Tellinghuisen, T.L., Perera, R., Kuhn, R.J., 2001. Genetic and biochemical studies on the assembly of an enveloped virus. Genet. Eng. 23, 83–112.
Tharakaraman, K., Watanabe, S., Chan, K.R., Huan, J., Subramanian, V., Chionh, Y.H., Raguram, A., Quinlan, D., McBee, M., Ong, E.Z., Gan, E.S., Tan, H.C., Tyagi, A., Bhushan, S., Lescar, J., Vasudevan, S.G., Ooi, E.E., Sasisekharan, R., 2018. Rational Engineering and Characterization of an mAb that Neutralizes Zika Virus by Targeting a Mutationally Constrained Quaternary Epitope. Cell Host Microbe 23, 618–627. e616.
Therkelsen, M.D., Klose, T., Vago, F., Jiang, W., Rossmann, M.G., Kuhn, R.J., 2018. Flaviviruses have imperfect icosahedral symmetry. Proc. Natl. Acad. Sci. U. S. A. 115 (45), 11608–11612.
Tran, E.E., Simmons, J.A., Bartesaghi, A., Shoemaker, C.J., Nelson, E., White, J.M., Subramaniam, S., 2014. Spatial localization of the Ebola virus glycoprotein mucin-like domain determined by cryo-electron tomography. J. Virol. 88 (18), 10958–10962.
Turoňová, B., Sikora, M., Schürmann, C., Hagen, W.J.H., Welsch, S., Blanc, F.E.C., von Bülow, S., Gecht, M., Bagola, K., Hörner, C., van Zandbergen, G., Landry, J., de Azevedo, N.T.D., Mosalaganti, S., Schwarz, A., Covino, R., Mühlebach, M.D., Hummer, G., Krijnse Locker, J., Beck, M., 2020. In situ structural analysis of SARS-CoV-2 spike reveals flexibility mediated by three hinges. Science 370 (6513), 203–208. https://doi.org/10.1126/science.abd5223. Epub 2020 Aug 18. PMID: 32817270; PMCID: PMC7665311.
Tyagi, A., Ahmed, T., Shi, J., Bhushan, S., 2020. A complex between the Zika virion and the Fab of a broadly cross-reactive neutralizing monoclonal antibody revealed by cryo-EM and single particle analysis at 4.1 A resolution. J. Struct. Biol. X 4, 100028.
Van Heel, M., 1987a. Similarity measures between images. Ultramicroscopy 21, 95–100.
Van Heel, M., 1987b. Angular reconstitution: a posteriori assignment of projection directions for 3D reconstruction. Ultramicroscopy 21, 111–123.
van Heel, M., Harauz, G., Orlova, E.V., Schmidt, R., Schatz, M., 1996. A new generation of the IMAGIC image processing system. J. Struct. Biol. 116, 17–24.
Van Heel, M., Gowen, B., Matadeen, R., Orlova, E.V., Finn, R., Pape, T., Cohen, D., Stark, H., Schmidt, R., Schatz, M., 2000. Single-particle electron cryo-microscopy: towards atomic resolution. Q. Rev. Biophys. 33, 307–369.
Vogel, R., Provencher, S., Von Bonsdorff, C.-H., Adrian, M., Dubochet, J., 1986. Envelope structure of Semliki Forest virus reconstructed from cryo-electron micrographs. Nature 320, 533–535.
Von Bonsdorff, C., Harrison, S., 1975. Sindbis virus glycoproteins form a regular icosahedral surface lattice. J. Virol. 16, 141–145.
Wahlberg, J.M., Garoff, H., 1992. Membrane fusion process of Semliki Forest virus. I: Low pH-induced rearrangement in spike protein quaternary structure precedes virus penetration into cells. J. Cell Biol. 116 (2), 339–348.
Wan, W., Clarke, M., Norris, M.J., Kolesnikova, L., Koehler, A., Bornholdt, Z.A., Becker, S., Saphire, E.O., Briggs, J.A., 2020. Ebola and Marburg virus matrix layers are locally ordered assemblies of VP40 dimers. Elife 9.
Wang, Q., Yang, H., Liu, X., Dai, L., Ma, T., Qi, J., Wong, G., Peng, R., Liu, S., Li, J., Li, S., Song, J., Liu, J., He, J., Yuan, H., Xiong, Y., Liao, Y., Li, J., Yang, J., Tong, Z., Griffin, B.D., Bi, Y., Liang, M., Xu, X., Qin, C., Cheng, G., Zhang, X., Wang, P., Qiu, X., Kobinger, G., Shi, Y., Yan, J., Gao, G.F., 2016. Molecular determinants of human neutralizing antibodies isolated from a patient infected with Zika virus. Sci. Transl. Med. 8 (369), 369ra179.
Wang, X., Li, S.H., Zhu, L., Nian, Q.G., Yuan, S., Gao, Q., Hu, Z., Ye, Q., Li, X.F., Xie, D.Y., Shaw, N., Wang, J., Walter, T.S., Huiskonen, J.T., Fry, E.E., Qin, C.F., Stuart, D.I., Rao, Z., 2017. Near-atomic structure of Japanese encephalitis virus reveals critical determinants of virulence and stability. Nat. Commun. 8, 14.
Wang, M., Sun, Z., Cui, C., Wang, S., Yang, D., Shi, Z., Wei, X., Wang, P., Sun, W., Zhu, J., Li, J., Du, B., Liu, Z., Wei, L., Liu, C., He, X., Wang, X., Zhang, X., Wang, J., 2022c. Structural insights into alphavirus assembly revealed by the Cryo-EM structure of Getah virus. Viruses 14.
Wang, A., Zhou, F., Liu, C., Gao, D., Qi, R., Yin, Y., Liu, S., Gao, Y., Fu, L., Xia, Y., Xu, Y., Wang, C., Liu, Z., 2022a. Structure of infective Getah virus at 2.8 A resolution determined by cryo-electron microscopy. Cell. Discovery 8, 12.
Wang, A., Zhou, F., Liu, C., Gao, D., Qi, R., Yin, Y., Liu, S., Gao, Y., Fu, L., Xia, Y., Xu, Y., Wang, C., Liu, Z., 2022b. Structure of infective Getah virus at 2.8 Å resolution determined by cryo-electron microscopy. Cell. Discovery 8, 12.
Weaver, S.C., Ferro, C., Barrera, R., Boshell, J., Navarro, J.-C., 2004. Venezuelan equine encephalitis. Annual Reviews in Entomology 49, 141–174.
Williamson, L.E., Bandyopadhyay, A., Bailey, K., Sirohi, D., Klose, T., Julander, J.G., Kuhn, R.J., Crowe Jr., J.E.J.P.o.t.N.A.o.S., 2023. Structural constraints link differences in neutralization potency of human anti-Eastern equine encephalitis virus monoclonal. antibodies 120, e2213690120.
Williamson, L.E., Gilliland Jr., T., Yadav, P.K., Binshtein, E., Bombardi, R., Kose, N., Nargi, R.S., Sutton, R.E., Durie, C.L., Armstrong, E., Carnahan, R.H., Walker, L.M., Kim, A.S., Fox, J.M., Diamond, M.S., Ohi, M.D., Klimstra, W.B., Crowe Jr., J.E., 2020. Human antibodies protect against aerosolized eastern equine encephalitis virus infection. Cell 183, 1884–1900.
Yao, H., Song, Y., Chen, Y., Wu, N., Xu, J., Sun, C., Zhang, J., Weng, T., Zhang, Z., Wu, Z., Cheng, L., Shi, D., Lu, X., Lei, J., Crispin, M., Shi, Y., Li, L., Li, S., 2020. Molecular architecture of the SARS-CoV-2 virus. Cell 183 (3), 730–738.e13. https://doi.org/10.1016/j.cell.2020.09.018. Epub 2020 Sep 6. PMID: 32979942; PMCID: PMC7474903.
Yap, M.L., Klose, T., Urakami, A., Hasan, S.S., Akahata, W., Rossmann, M.G., 2017. Structural studies of Chikungunya virus maturation. Proc. Natl. Acad. Sci. U. S. A. 114 (52), 13703–13707.
Yu, I.-M., Zhang, W., Holdaway, H.A., Li, L., Kostyuchenko, V.A., Chipman, P.R., Kuhn, R.J., Rossmann, M.G., Chen, J., 2008. Structure of the immature dengue virus at low pH primes proteolytic maturation. Science 319, 1834–1837.
Zhang, K., 2016. Gctf: Real-time CTF determination and correction. J. Struct. Biol. 193, 1–12.
Zhang, R., Hryc, C.F., Cong, Y., Liu, X., Jakana, J., Gorchakov, R., Baker, M.L., Weaver, S. C., Chiu, W., 2011a. 4.4 A cryo-EM structure of an enveloped alphavirus Venezuelan equine encephalitis virus. EMBO J. 30, 3854–3863.
Zhang, R., Hryc, C.F., Cong, Y., Liu, X., Jakana, J., Gorchakov, R., Baker, M.L., Weaver, S. C., Chiu, W., 2011b. 4.4 Å cryo-EM structure of an enveloped alphavirus Venezuelan equine encephalitis virus. EMBO J. 30, 3854–3863.
Zhang, S., Kostyuchenko, V.A., Ng, T.-S., Lim, X.-N., Ooi, J.S.G., Lambert, S., Tan, T.Y., Widman, D.G., Shi, J., Baric, R.S., Lok, S.-M., 2016. Neutralization mechanism of a highly potent antibody against Zika virus. Nat. Commun. 7, 13679.
Zhang, S., Loy, T., Ng, T.S., Lim, X.N., Chew, S.V., Tan, T.Y., Xu, M., Kostyuchenko, V.A., Tukijan, F., Shi, J., Fink, K., Lok, S.M., 2020. A Human Antibody Neutralizes Different Flaviviruses by Using Different Mechanisms. Cell Rep. 31, 107584.
Zhang, W., Mukhopadhyay, S., Pletnev, S.V., Baker, T.S., Kuhn, R.J., Rossmann, M.G., 2002. Placement of the structural proteins in Sindbis virus. J. Virol. 76, 11645–11658.
Zhang, W., Chipman, P.R., Corver, J., Johnson, P.R., Zhang, Y., Mukhopadhyay, S., Baker, T.S., Strauss, J.H., Rossmann, M.G., Kuhn, R.J., 2003a. Visualization of membrane protein domains by cryo-electron microscopy of dengue virus. Nat. Struct. Mol. Biol. 10, 907–912.
Zhang, Y., Corver, J., Chipman, P.R., Zhang, W., Pletnev, S.V., Sedlak, D., Baker, T.S., Strauss, J.H., Kuhn, R.J., Rossmann, M.G., 2003b. Structures of immature flavivirus particles. EMBO J 22, 2604–2613.
Zhang, X., Sheng, J., Plevka, P., Kuhn, R.J., Diamond, M.S., Rossmann, M.G., 2013a. Dengue structure differs at the temperatures of its human and mosquito hosts. Proceedings of National Academy of Sciences 110, 6795–6799.
Zhang, X., Ge, P., Yu, X., Brannan, J.M., Bi, G., Zhang, Q., Schein, S., Zhou, Z.H., 2013b. Cryo-EM structure of the mature dengue virus at 3.5-A resolution. Nat. Struct. Mol. Biol. 20, 105–110.
Zheng, S.Q., Palovcak, E., Armache, J.P., Verba, K.A., Cheng, Y., Agard, D.A., 2017. MotionCor2: anisotropic correction of beam-induced motion for improved cryo-electron microscopy. Nat Methods 14, 331–332.
Zhou, Q.F., Fox, J.M., Earnest, J.T., Ng, T.-S., Kim, A.S., Fibriansah, G., Kostyuchenko, V. A., Shi, J., Shu, B., Diamond, M.S., 2020a. Structural basis of Chikungunya virus inhibition by monoclonal antibodies. Proceedings of National Academy of Sciences 117, 27637–27645.
Zhou, Q.F., Fox, J.M., Earnest, J.T., Ng, T.S., Kim, A.S., Fibriansah, G., Kostyuchenko, V. A., Shi, J., Shu, B., Diamond, M.S., Lok, S.M., 2020b. Structural basis of Chikungunya virus inhibition by monoclonal antibodies. Proceedings of National Academy of Sciences 117, 27637–27645.
Zhu, D., Wang, X., Fang, Q., Van Etten, J.L., Rossmann, M.G., Rao, Z., Zhang, X., 2018. Pushing the resolution limit by correcting the Ewald sphere effect in single-particle Cryo-EM reconstructions. Nat. Commun. 9, 1552.
Zivanov, J., Nakane, T., Forsberg, B.O., Kimanius, D., Hagen, W.J., Lindahl, E., Scheres, S.H., 2018. New tools for automated high-resolution cryo-EM structure determination in RELION-3. Elife 7, e42166.